POLITECNICO
MILANO 1863

SCUOLA DI INGEGNERIA INDUSTRIALE
E DELL'INFORMAZIONE

Precise emission wavelength adjustment in lead halide perovskites using a gas-solid phase reaction with parylene-C

TESI DI LAUREA MAGISTRALE IN
CHEMICAL ENGINEERING
INGEGNERIA CHIMICA

Author: **Oliviero Bacci**

Student ID: 10720405
Advisor: Prof. Dr. Chih-Jen Shih, ETH Zurich
Advisor: Prof. Dr. Giuseppe Storti
Co-advisor: Gerrit Stemmler, ETH Zurich
Academic Year: 2024-25

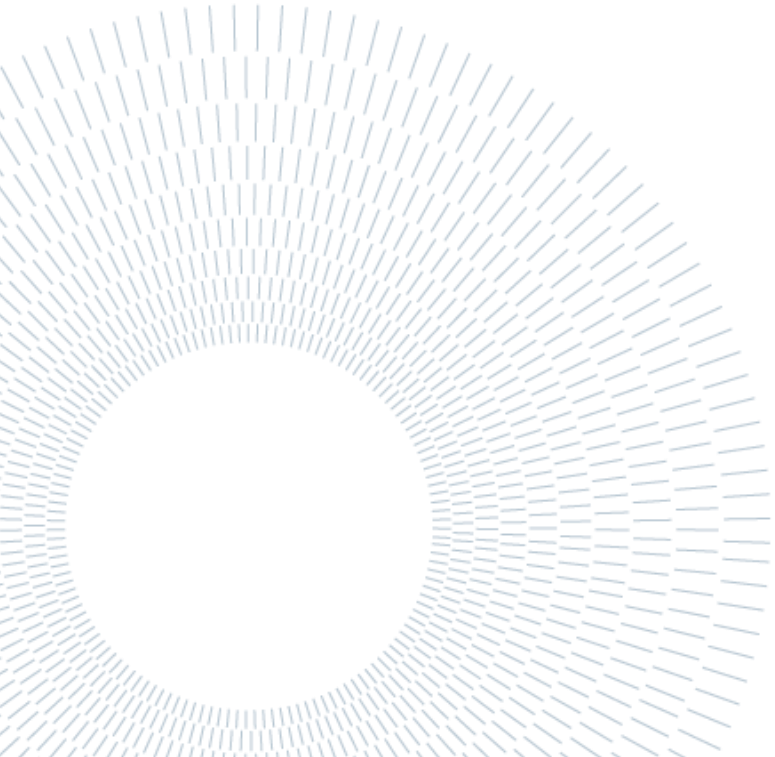

Abstract

This thesis explores the precise emission wavelength adjustment in lead halide perovskites (LHPs) using a gas-solid phase reaction facilitated by parylene-C. Lead halide perovskite nanocrystals (NCs) are highlighted for their exceptional photoluminescent properties and potential applications in optoelectronics, including LEDs, photodetectors, and lasers. The work aims to achieve a controlled shift from green to blue emission through a novel solid-gas-phase ion-exchange process during parylene deposition.

Key findings include the identification of diffusion limitations and their solutions, as well as the development of a numerical prediction model to optimize the ion exchange process. The research demonstrates significant advancements in the stability and efficiency of blue-emitting LHP NCs, paving the way for their broader application in cost-effective, high-performance optoelectronic devices.

Key-words: lead halide perovskites, parylene, gas-solid phase reaction, diffusion control, pure blue emission control.

Sommario

Questa tesi esplora la precisa regolazione della lunghezza d'onda di emissione nei perovskiti alogenuri di piombo (LHP) mediante una reazione in fase solido-gas facilitata da parylene-C. I nanocristalli (NC) di perovskite alogenuri di piombo sono messi in evidenza per le loro eccezionali proprietà fotoluminescenti e per le potenziali applicazioni in optoelettronica, tra cui LED, fotodetettori e laser. Il lavoro si propone di ottenere uno spostamento controllato dall'emissione verde a quella blu attraverso un innovativo processo di scambio ionico in fase solido-gas durante la deposizione del parylene.
I risultati chiave includono l'identificazione delle limitazioni dovute alla diffusione e le relative soluzioni, nonché lo sviluppo di un modello numerico predittivo per ottimizzare il processo di scambio ionico. La ricerca dimostra significativi progressi nella stabilità e nell'efficienza dei NC LHP a emissione blu, aprendo la strada a una loro più ampia applicazione in dispositivi optoelettronici ad alte prestazioni e basso costo.

Parole chiave: perovskiti alogenuri di piombo, parilene-C, reazione in fase solido-gas, controllo della diffusione, controllo dell'emissione blu pura.

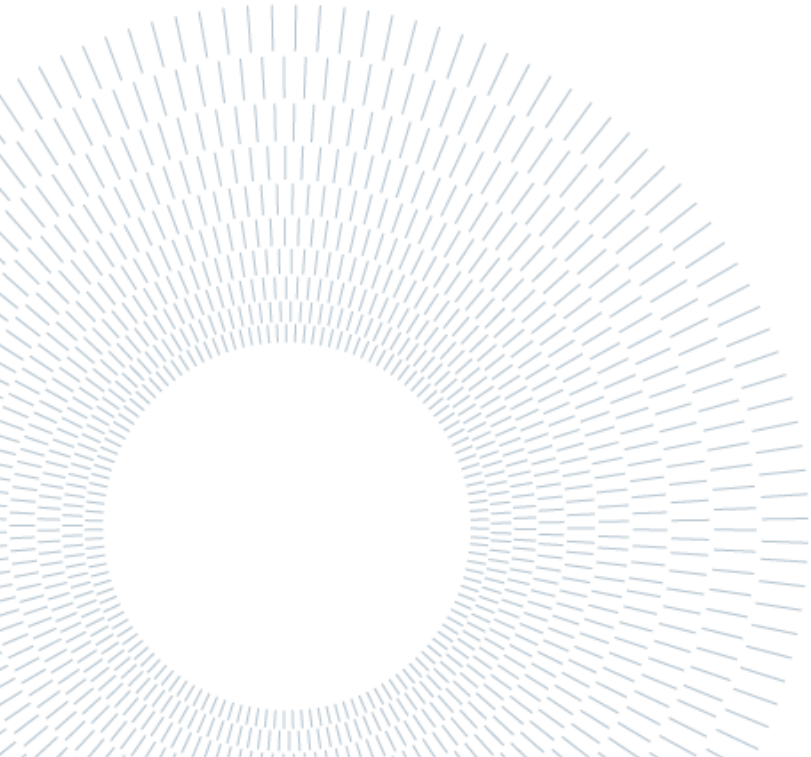

Contents

1 Introduction

Lead halide perovskite nanocrystals (NCs) are emerging as a revolutionary class of materials in the world of nanotechnology due to their exceptional properties and versatile applications. These colloidal semiconductor nanocrystals, which range in size from 4 to 15 nanometers, have captivated researchers with their remarkable ability to emit intensely bright and pure colour [1]. Their photoluminescence is not only bright but also tuneable across a wide range of colours by simply altering their composition or size. This colour tunability, spanning a spectrum from 410 to 700 nanometers, can be achieved directly through synthesis, or via ion exchange in solution [2] or gas-phase reactions. Such a broad spectrum is incredibly useful for various applications in the optoelectronics field, particularly in light-emitting diodes (LEDs) [3], [4], [5], [6], photodetectors [7], [8], lasers [9], transistors [10] and photocatalysts . However, despite their potential, current optoelectronic devices predominantly utilize green-emitting perovskites due to their greater stability. The implementation of blue-emitting perovskites remains challenging because of the higher quantity and depth of trap states that are present in them.

What makes lead halide perovskite NCs particularly fascinating is their simple and scalable synthesis [11], [12]. They can be produced using straightforward chemical processes, which allows for large-scale manufacturing without the need for complex or expensive equipment. This ease of production, combined with their inherent high efficiency and low cost of materials, positions them as a promising material for cost-effective applications across various fields. The narrow emission spectra defined as full width at half maximum (FWHM) that can be obtained with high size monodispersity [13] allows to obtain high colour purity in the emission. The ability to produce blue-emitting lead halide perovskites (LHPs) efficiently and at scale is crucial, making them a standout material for future technological advancements, especially where performance and cost-effectiveness are essential.

The aim of this thesis is to achieve a controlled colour shift from green emitting LHP-NCs to blue through gas-phase ion exchange, carried out by parylene deposition.

1.1. Metal Halide Perovskites

The earliest research work on metal-halide perovskites (MHPs) was conducted in the late 1800s by Wells [14], while the detailed structural characterization was carried out by Weber in the 1900s [15], [16], [17]. Their potential applications in electronic and

optical devices attracted attention in the late 1990s and the early 2000s, long before captivating the broad scientific community [18], [19]. The optical and electronic properties of MHPs were shown to be strongly dependent on their dimensionality (both structural and morphological).

Three-dimensional (3D) MHPs refer to a class of crystalline compounds adopting the generic chemical formula ABX_3, where the cation "B" has six nearest-neighbour anions "X", while the cation "A" sits in a cavity formed by eight corner-sharing BX6 octahedra [20].

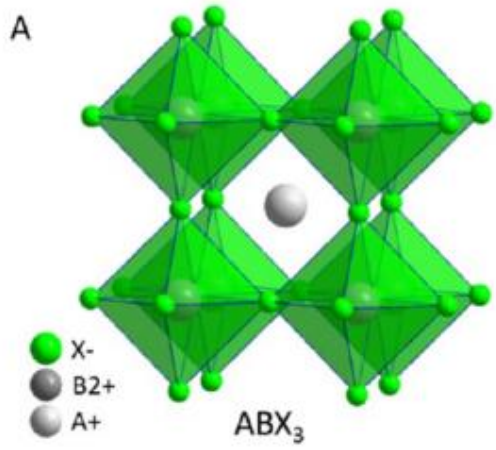

Figure 1.1: Illustration of 3D perovskite structure

LHPs are generally classified into either organic–inorganic hybrid (OIH) [21] or inorganic perovskites depending on whether the A-site cation is organic or inorganic. OIH perovskites generally have methylammonium (MA) or/and formamidinium (FA) as the monovalent A-site cation, lead as the divalent B cation and chlorine, bromine, iodine, or their combinations as the halide ion (X). On the other hand, inorganic perovskites have cesium (Cs) or rubidium (Rb) as the A cation. The ideal structure of the perovskite, which is illustrated in Figure 1.1, is based on a cubic lattice. However, the deviation from the ideal perovskite structure in ABX_3 materials can be predicted through the Goldschmidt tolerance factor t ($t = (rA + rX)/[\sqrt{2}(rB + rX)]$), where rA, rB, and rX are the ionic radii of the corresponding ions, and t is defined as the ratio of the distance A–X to the distance B–X.

Bulk perovskites suffer from low photoluminescence quantum yields (PLQYs) due to inherent defects, particularly those present at grain boundaries, surfaces, and interfaces [22], [23], [24]. On the other hand, MHP NCs appeared as extremely efficient light emitters with near-unity PLQY and narrow spectrum emission. These colloidal suspensions are stabilized by ligands, which act as surfactants in a liquid-liquid emulsion. They have a surface passivation role, closing some present trap state and increasing the PLQY due to the less presence of trap states[25], and they put a steric activation energy between NCs slowing down the aggregation kinetics, improving the

colloidal stability [26]. The ligands play also a crucial roles also during synthesis controlling the final size and shape of NCs [27].

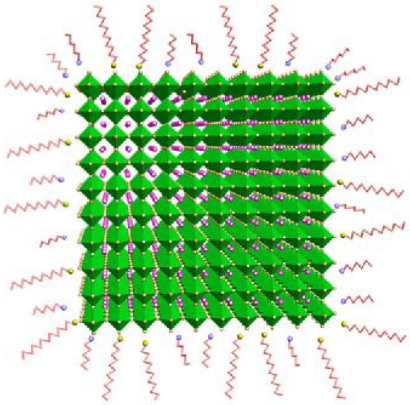

Figure 1.2: Ligands position in a colloidal solution of LHP-NCs

The optical properties of LHPs are closely connected to the difference in energy between valence band and conductive band. The emitted wavelength is tunable across the visible spectrum of light by simply varying the ratio between the halides [2], [28], [29], [30]. Changing the halide component (e.g., from iodide to bromide or chloride) shifts the band gap, altering the emission wavelength. This tunability is crucial for tailoring materials for specific optoelectronic applications, such as creating LEDs with different colours.

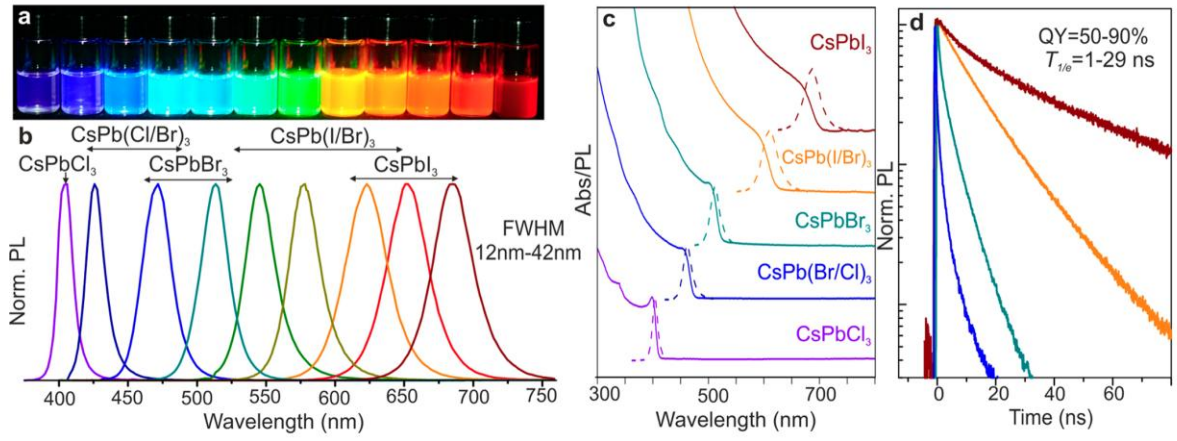

Figure 1.3: Colloidal perovskite $CsPbX_3$ NCs (X = Cl, Br, I) exhibit size- and composition-tunable bandgap energies covering the entire visible spectral region: a) colloidal solutions in toluene under UV lamp (λ = 365 nm); b) representative PL spectra; c) typical optical absorption and PL spectra for non-quantum confinement NCs; (d) time-resolved PL decays for all samples shown in c) except $CsPbCl_3$ [1] .

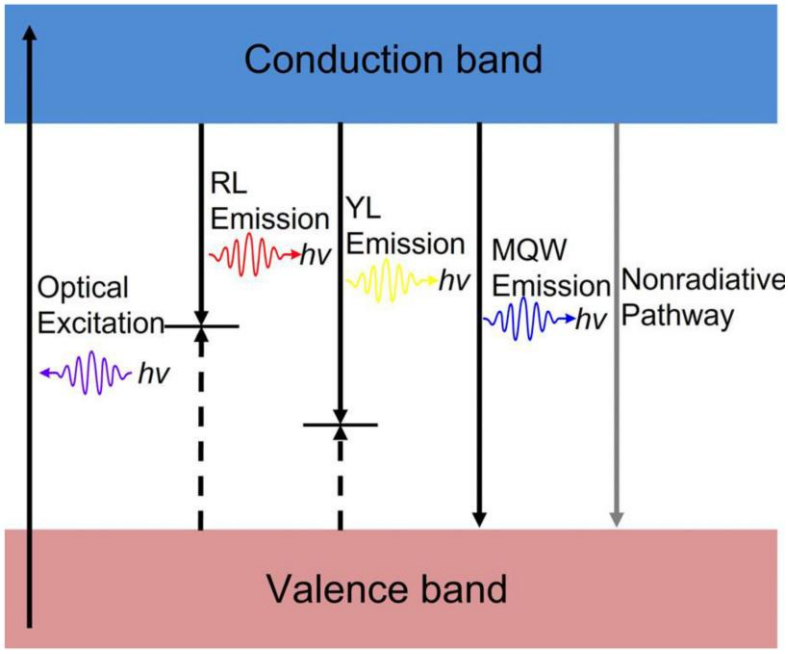

Figure 1.4: Representative diagram of recombination through three luminescent pathways that lead to different colours. The dotted and grey lines represent non radiative pathways.

As can be seen in Figure 1.4 the difference in energy emitted by radiation directly influence the wavelength.

1.1.1. Quantum confinement

The bulk properties of MHP are significant, decreasing the size of the crystals to the nanoscale reveals their size-dependent optical and electronic properties. For instance, nanosized crystals exhibit quantum confinement effects that can be exploited to tune the optical properties, [1], [31], [32], [33] much like in other semiconductors.[34], [35]. When the particle size of the semiconductors is reduced up to the nanometers scale quantum confinement occurs and the electronic and optoelectronic properties become dependent on their size and shape [36], [37]. Such particles are usually called Quantum dots (QDs) or artificial atoms due to their discrete (quantized) density of energy states like in actual atoms [38], [39].

One of the main QDs characteristics is the size-dependent bandgap which can be tuned in the whole range of colours between ultraviolet and infrared [40], [41](depending on the semiconductor material). With proper control in the surface chemistry it is possible to obtain low defect QDs with bright emission and high photoluminescence quantum yield (PLQY) [42], [43], [44]. LEDs that exploit QDs as light emitting material (QD-LEDs) show higher colour purity and brighter luminescence than organic based LED (OLEDs) [45] making them a promising technology to meet Rec. 2100 colour gamut specifications [46].

A quantum confined NCs has a different behaviour with respect to a LHP-NCs. In normal MHPs the changing in colour is only related to the halogen ratio inside the NCs, while in QDs it is also strictly connected to dimension. Changing the dimension (3-8 nm) the emitted wavelength, energy emitted, change accordingly [47], [48].

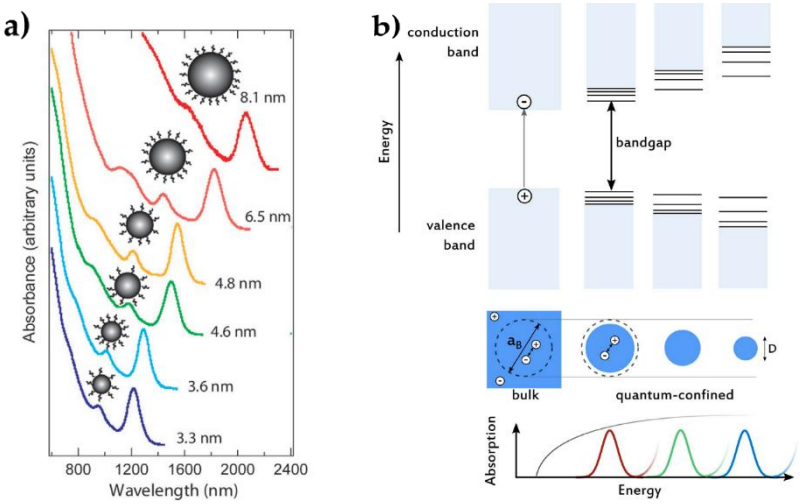

Figure 1.5: a) Absorbance spectra of quantum confinement QDs varying the size[48]; b)quantum confinement effect on QDs leading on a change in bandgap energy, and so in colour emitted[47]

1.1.2. Trap state

LHPs ability to emit light efficiently is intrinsically linked to the interplay of band gap theory and trap state theory. In semiconductors, like LHPs, the band gap is the energy difference between the valence band (highest energy of electrons at rest) and the conduction band, lowest energy level that electrons can move into when excited. When an electron absorbs energy, such as from light, it can be excited from the valence band to the conduction band, leaving behind a hole in the valence band. When these excited electrons recombine with the holes, energy is released, in the form light (photon emission) or through non-radiative recombination pathways, like heat generation. The less is the energy dispersed by heat the higher will be the efficiency of the light emission [49], [50].

Trap states are defects or impurities within the material that create localized energy states within the band gap. These trap states can capture and hold charge carriers (electrons or holes), affecting the efficiency of light emission acting as a non-radiative recombination centre where the trapped charged recombine without emitting photons or emitting an energy lower the one that a free excitons can emit [51], [52], [53]. They are often associated with the presence of surface defects or grain boundaries.

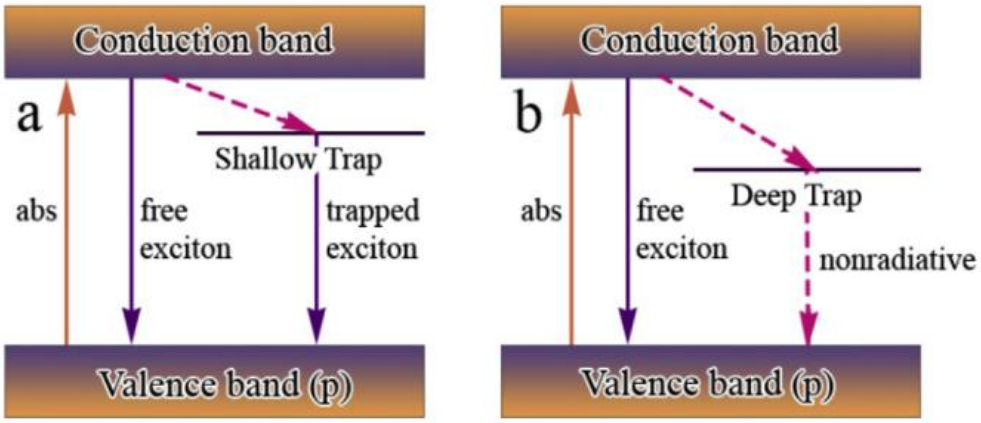

Figure 1.6: Scheme of radiative (a) and non-radiative (b) trapping of electrons. Dash lines represent non radiative pathways instead the solid is related to photons emission [51].

Reducing trap states is essential for enhancing the photoluminescence efficiency of LHPs [54]. Some strategies include surface passivation [55], synthesis optimization and improve the crystallinity. These approaches help to increase the radiative recombination rate and suppress non-radiative pathways, thereby boosting light emission.

1.2. Blue LHP-NCs synthetic technics

In this chapter are shown all the main techniques used to cover all the RGB spectrum. These are divided into two main groups: Direct synthetic pathways and ion-exchange after colloidal synthesis.

1.2.1. Direct synthetic pathways

All the synthesis methods for monodispersed $CsPbX_3$ typically take advantage of the ionic nature of the chemical bonding in these compounds. Direct synthesis, in this context, refers to the straightforward chemical processes where precursor materials react directly to form $CsPbX_3$ nanocrystals. This approach often involves the precise control of reaction conditions such as temperature, concentration, and reaction time to ensure the uniform size and composition of the resulting nanocrystals. By leveraging the ionic bonding characteristics, these synthesis methods can produce high-quality, monodispersed nanocrystals with desirable optical and electronic properties.

1.2.1.1. Hot Injection

This synthesis is a controlled arrested precipitation of Cs^+, Pb^{2+} and X^- ions into $CsPbX_3$ NCs. It is known for obtaining NCs with narrow emission line, 12 nm for X=Cl, 42 nm for X=I, and high quantum yields between 50-90% based on halide composition [1]. The ligands usually used are oleylamine and oleic acid in ratio 1:1, which inhibits the

application in LEDs due to the high resistance that they apply to electron conductivity. The reaction combines PbX_2 with Cs-oleate at high temperature. Different emission wavelengths are easily obtained combining appropriate ratio of PbX_2 salts (Figure 1.7). Cl/I perovskites cannot be obtained due to the large difference in ionic radii, which is in accord with the phase diagram for bulk materials [56].

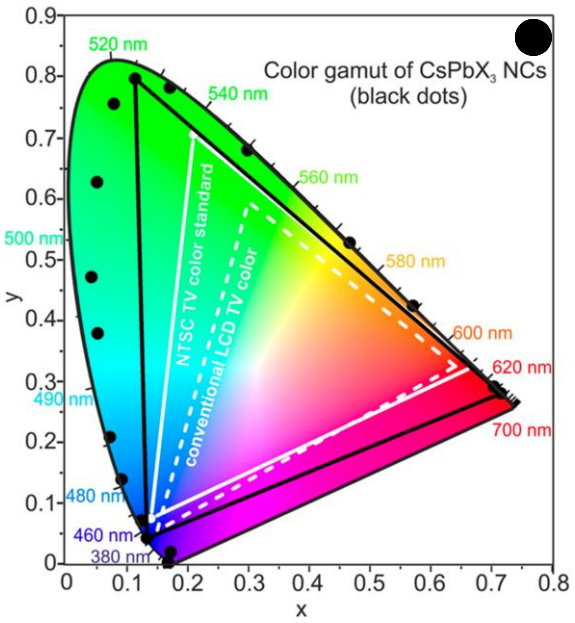

Figure 1.7: Emission from $CsPbX_3$ NCs (black dots) plotted in chromaticity diagram[1]

1.2.1.2. Solvothermal methods

Solvothermal synthesis is an effective method for producing lead halide perovskite nanocrystals (LHP NCs). Unlike traditional techniques like hot injection, which operate at atmospheric pressure and require precise control of injection and temperature, solvothermal methods use high temperatures and pressures in a closed system. This allows better control over the crystallization process, leading to precise tuning of size, shape, and composition of the nanocrystals. In a typical solvothermal synthesis, precursors such as $PbCl_2$ and CsCl are dissolved in solvents like oleic acid and oleylamine and heated in an autoclave at 150-200°C to produce high-quality blue-emitting $CsPbCl_3$ nanocrystals [57]. This method provides excellent control over nanocrystal properties due to the controlled high-pressure environment.

Alternatively, a low-temperature solvothermal approach uses dimethylformamide (DMF) as a solvent at moderate temperatures (100-120°C), which helps in forming $CsPbCl_3$ nanocrystals with desired blue emission characteristics while maintaining their structural integrity [58]. Unique adaptations, such as using alkylamines as solvents, can coordinate with lead halides to manage crystal growth. This approach has been used to synthesize $CsPbX_3$ (X = Cl, Br, I) nanocrystals with precise control over size and optical properties, essential for achieving efficient blue emission [59].

Combining hydrothermal and solvothermal methods, where an aqueous solution of $PbCl_2$ and CsCl is heated in an autoclave, also produces luminescent blue-emitting $CsPbCl_3$ nanocrystals, benefiting from the solvent's ability to dissolve and distribute precursors evenly in a high-pressure environment [60].

1.2.1.3. Microwave assisted synthesis

Microwave-assisted synthesis is an advanced method for producing lead halide perovskite nanocrystals (LHP NCs), especially effective for crafting blue-emitting variants. This technique uses microwave radiation to heat the reaction mixture rapidly and uniformly, enhancing reaction kinetics and significantly shortening synthesis times compared to traditional methods like solvothermal or hot injection techniques. The accelerated and uniform heating facilitates controlled nucleation and growth of the nanocrystals, resulting in products with precise size, shape, and optical properties[61]. . A complex reaction setup, such as inert atmosphere and high reaction temperature, are not required for this synthesis. As a comparison, the optical properties of ABX_3 perovskite NCs are mainly determined by their composition rather than size and shape. If the size is larger than the Bohr radius, it suggests better reproducibility.

Combining microwave irradiation with the presence of surfactants like oleylamine and oleic acid can also produce $CsPbX_3$ (X = Cl, Br, I) nanocrystals with tailored optical properties. This technique benefits from the microwave's ability to provide rapid and homogeneous heating, allowing for the quick and efficient synthesis of nanocrystals with tunable emission properties [62].

1.2.1.4. Ligand assisted reprecipitation (LARP)

Ligand-Assisted Reprecipitation (LARP) is a widely used technique for synthesizing lead halide perovskite nanocrystals (LHP NCs), particularly effective for producing both inorganic and hybrid inorganic-organic perovskites. This method involves the use of ligands, e.g. decylamine, to stabilize the nanocrystals during the rapid precipitation process, allowing for the creation of high-quality nanocrystals with controlled size and shape. This technique is highly adaptable, allowing for the synthesis of both purely inorganic (e.g., $CsPbX_3$) and hybrid inorganic-organic perovskites (e.g., $(MA/FA)PbX_3$, where MA = methylammonium and FA = Formamidinium) with diverse compositions and emission characteristics [62], [63], [64].

Figure 1.8: LARP synthesis approach [27]

The mixture of the two solvents induces an instantaneous supersaturation, which triggers the nucleation and the growth of perovskite NCs. It is straightforward to understand that, being the LARP synthesis carried out in air using a quite simple chemical apparatus, differently from the HI techniques, it can be easily scaled up, allowing for the large-scale production of MHP NCs, up to the gram scale [64], [65], [66].

1.2.2. Post synthetic anion exchange

This paragraph delves into the production of LHP-NCs with a broad colour spectrum using a different post-synthetics reaction. The starting point, in any of these techniques, is to have already synthetized nanocrystals. All of them aim to perform the halides exchange in existing NC structure to modulate the emitted wavelength.

1.2.2.1. Anion Exchange in Solution

The anion-exchange reaction is conducted starting from $CsPbX_3$ in dry octadecene (ODE) as a solvent. It can be performed at low temperature choosing a correct amount of halogen source. Modulating the time is possible to have a complete or a partial conversion in solution. It is easily performed in the case of Cl-to-Br, Br-to-Cl and I-to-Br via the formation of a homogeneous solution. No mixed-halide solution Cl-to-I, or the other way around, are possible due to the substantial difference in molecular radii. Only a slow and complete conversion can be obtained between these two halogens [2],[67].

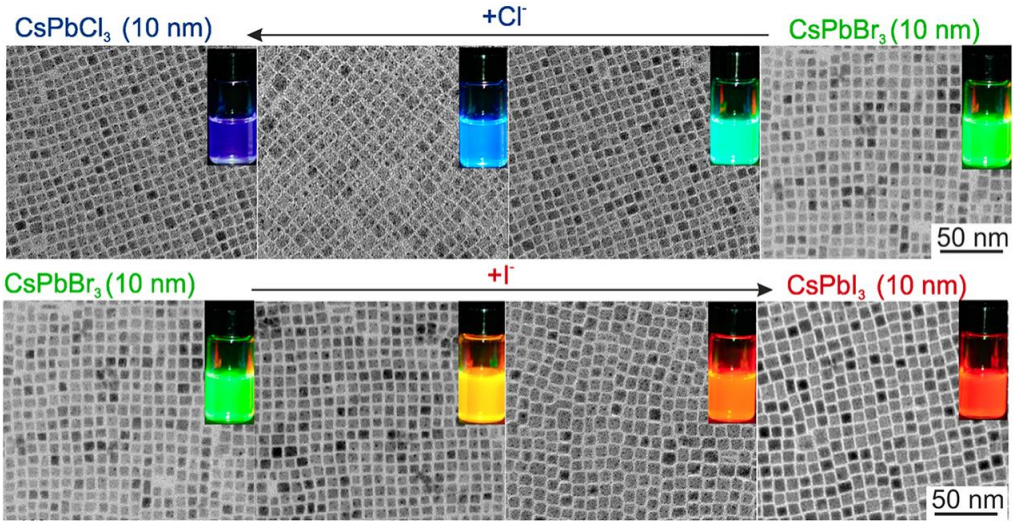

Figure 1.9: Evolution of emission colours coupled by transmission electron microscopy (TEM) images [2].

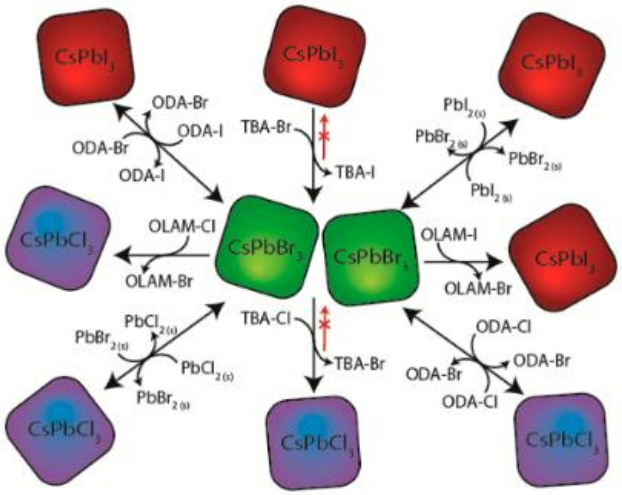

Figure 1.10: Overview of the Different Routes and Precursors for the Anion Exchange Reactions [30].

The size and shape of the parent NCs are preserved in the course of the anion-exchange (Figure 1.10) [30]. The direct synthesis of single or mixed-halide $CsPbX_3$ at low temperatures yields either exclusively large and polydisperse crystallites of poorly or non-luminescent, wider-bandgap orthorhombic phases or simply no crystalline products at all. $CsPbI_3$, for example, is highly luminescent and red in its three-dimensional cubic phase, yet yellow and non-luminescent upon conversion into its orthorhombic polymorph [56], [68], [69], [70].

1.2.2.2. Photoluminescence Induced Exchange

Photoluminescence induced exchange of a $CsPbX_3$ solution of NCs suspended in dihalomethane. The extent of anion exchange reaction and its rate are controlled by

the intensity or the wavelength of light without any reactive sources of halide. dihalomethane is used as a halide source even it is usually used as a non rective solvent. It produce halide through a photoinduced electron transfer from NCs. The halide ions generated in situ near the surface of NCs drive the anion exchange reaction, as long as the CsPbX3 NCs are photoexcited above the bandgap [71].

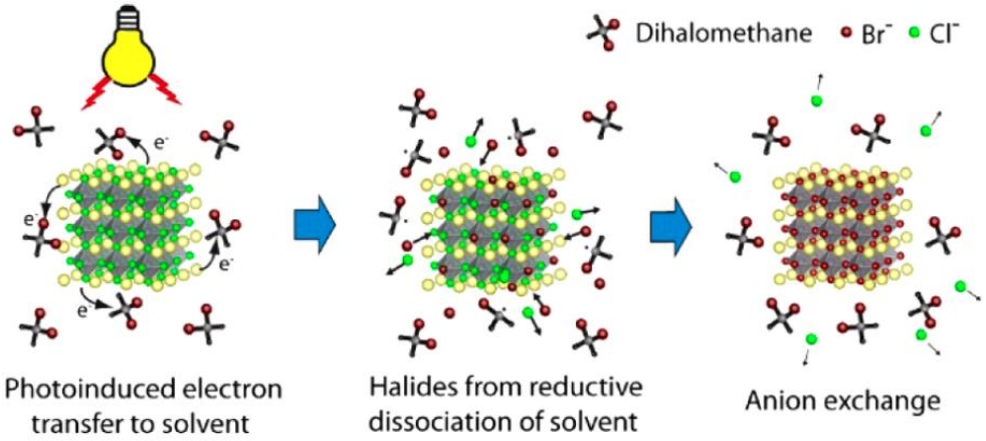

Figure 1.11: Photoinduced mechanism for photoinduced Anion Exchange [71].

The exchange of anions can occur in both directions changing the solvent composition and is strictly dependent on the illumination time.

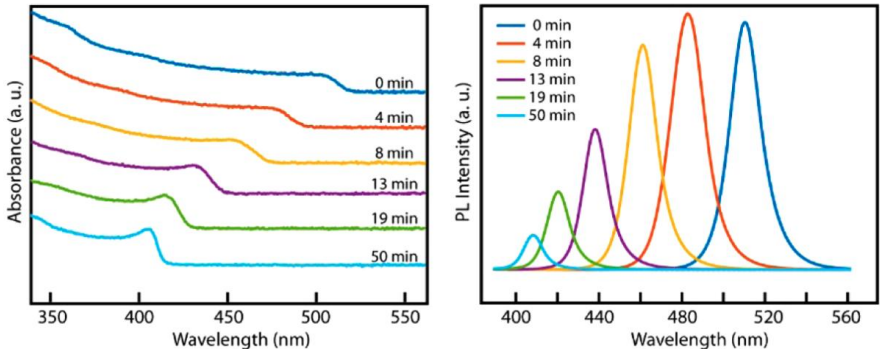

Figure 1.12: Photoinduced anion exchange in time keeping constant source parameters (405 nm light and ~20 mW/cm2)[71].

1.2.2.3. Gas-Solid Anion-Exchange Reaction

Exposing $CsPbX_3$ NCs to halide gases or halogen-containing vapours initiates a halide exchange process that begins at the nanocrystal surface and propagates inward [30]. This process is highly dependent on the diffusion of the gas-phase halogen into the solid crystal lattice. The kinetics of this solid-gas reaction are crucial for achieving uniform halide distribution and stable luminescent properties [71]. For instance, when $CsPbBr_3$ NCs are exposed to chlorine vapor, an anion exchange occurs where bromine is partially or fully replaced by chlorine, forming $CsPb(Br/Cl)_3$ or $CsPbCl_3$ NCs. The extent of this exchange and the resulting halide composition can be finely controlled by adjusting the chlorine vapor pressure and the reaction temperature.

Careful control of reaction conditions, such as the partial pressure of the gas and the temperature, plays a pivotal role in the efficiency and uniformity of the anion exchange [76]. Higher partial pressures can enhance the rate of diffusion, facilitating a more rapid and complete exchange, whereas temperature influences the mobility of the ions and the reaction kinetics. Precise management of these parameters allows for fine-tuning of the nanocrystal properties, enabling the production of materials with tailored optical characteristics for specific applications.

There are several advantages to this approach. One major benefit is the ability to precisely tune the optical properties of the nanocrystals by controlling the halide composition, which can be critical for applications in light-emitting diodes (LEDs), lasers, and photovoltaic cells. The gas-solid reaction method allows for post-synthesis modification of NCs, providing flexibility in the material design process. Unlike other methods, which may require extensive post-processing or complex chemical alterations, this technique offers a straightforward means to adjust the material properties through controlled exposure to halide gases.

Moreover, this method can be more industrially viable compared to alternative strategies. By employing a gas-phase reaction, it is possible to achieve a wide gamut of colours with high precision, which is crucial for applications that demand exacting colour requirements. This is particularly beneficial in commercial applications where a consistent and controllable range of optical properties is needed. Additionally, the direct exchange on thin films can open up new ways in fabrication processes for LHP-based optoelectronic devices, by enabling post-synthetic colour-tuning during manufacturing steps.

1.3. Parylene

The following sub-charter delves into the presentation of Parylene including polymerization aspects, reactivity, application and Parylene CVD.

1.3.1. Parylene Family

Parylene is a generic name for members of a polymer series generally referred to poly(para-xylylene). It can contain chlorine, fluorine or it can be halogen free. There are three members of this family: parylene-C, parylene-D, parylene-N, that are the most used, and parylene-HT [72].

- Parylene-N: It is the simplest member, It is characterized by a completely linear structure due to the absence of halides and an high crystallinity. It stands out as a primary dielectric due to its low dissipation factor, high dielectric strength, and a dielectric constant that remains stable across varying frequencies.

- **Parylene C**: It is the second variant in the series, is synthesized from the same dimer as Parylene N but with a chlorine atom replacing one of the aromatic hydrogens. The feedstock raw material is called DPX-C (Figure 1.13), a closed dimer of chlorine para-xylylene. This modification provides Parylene C with a unique blend of electrical and physical properties, along with very low permeability to moisture and corrosive gases.

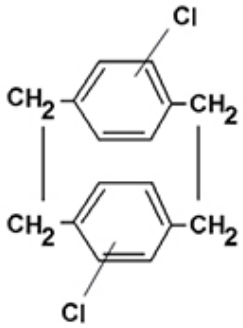

Figure 1.13: Structural formula of DPX-C dimer

- Parylene D: It is originated from a similar dimer as Parylene-C but with two chlorine atoms substituting for two aromatic hydrogens. It retains properties similar to Parylene C, but can withstand slightly higher temperatures.
- Parylene HT: It is quite similar to the Parylene-N but with fluorine that substitutes the hydrogen in alpha position. This modification makes Parylene HT suitable for high-temperature applications (up to 450°C short-term) and environments requiring long-term UV stability. It also boasts the lowest coefficient of friction and dielectric constant, as well as the highest crevice-penetration ability among the four variants [72].

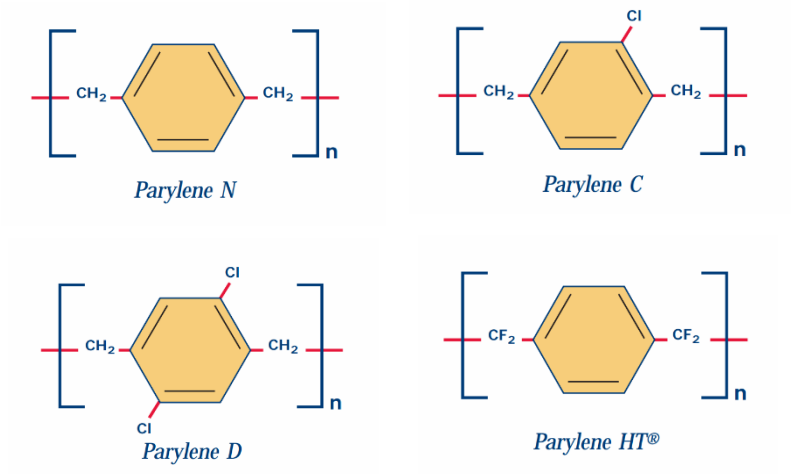

Figure 1.14: Members of parylene family[72]

Parylene polymers, thanks to a chemical vapor-phase deposition process, can form continuous films ranging from just a few nanometers to 75 microns in thickness[72].

1.3.2. Polymerization

Parylenes have to be polymerized in situ and cannot be formed by extrusion or moulding technics due to their high melting temperature and crystallinity since that their molecular weight is around 5*10^5 Da. The polymerization takes place in vacuo without any catalyst. It is divided in three steps as in a normal free radical polymerization reaction: initiation, propagation and termination.

Initiation part is the formation of biradical species through pyrolytic decomposition of the starting material. In the case of Parylene-C the starting material is DPX-C, which is divided into a biradical and a quinoidal structure, that is a mesomeric form of the monomer (Figure 1.15).

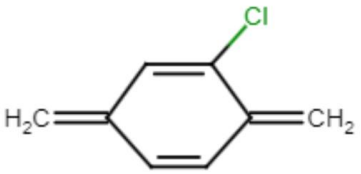

Figure 1.15: Mesomeric form of the monomer

The monomers after pyrolysis, when the temperature is lowered, do not re-form cyclic dimers but instead polymerize into long chain molecules (propagation step). The initiation of polymerization requires dimerization of two monomers leading to formation of a noncoupled biradical dimer. The chain molecules grow through the propagation reaction only one unit at a time, by the attachment of a monomer to a radical chain end [73].

1.3.3. Overview on Chemical Vapor Deposition (CVD)

In a general CVD process the deposition of a solid film occurs through a substrate surface reaction:

$$A_g + B_g \rightarrow C_s + D_g \qquad \textbf{1.1}$$

Where A and B are the gaseous reactant, D the gaseous product and C is the solid deposited material.

The film deposition proceed in different steps:

1) Transport of the reactant in deposition chamber;
2) Diffusion of the reactant inside the chamber;
3) Adsorption of the reactant onto substrate surface;
4) Surface chemical reaction;
5) Surface migration and lattice incorporation;
6) Reaction product desorption;

7) Product diffusion away from the surface;
8) Transport of the product out of the deposition chamber.

These steps are in series and this mean that reaction rate is controlled by the slowest one. Reaction rate can be controlled by mass transport if step (1) or (8) are the rate limiting, by diffusion if step (2) or (7) are limiting and kinetic control if one between (3)-(6) is limiting.

The Parylene process is slightly different from that. There is only one gaseous reactant and no gaseous products. The initiation reaction takes place only when a minimum of three monomer molecules join to form a diradical oligomer [74].

$$3M_g \rightarrow P^*_{m=3,s} \quad \textbf{1.2}$$

Where M is the monomer and P is the polymer. The "*" refers to a di-radical. The propagation reaction is described by the following equation:

$$M_g + P^*_{m,s} \rightarrow P^*_{m+1,s} \quad \textbf{1.3}$$

The steps leading to Parylene deposition are different from the classical CVD process:

1) Transport of monomer into deposition chamber;
2) Monomer diffusion inside the chamber;
3) Adsorption of the monomer on the substrate;
4) Surface migration and possible bulk diffusion of monomer;
5) Chemical reaction.

The CVD process for Parylene has been experimentally determined to be kinetically controlled [75], [76], [77], [78], [79].

1.3.4. Parylene CVD Process

The Parylenes are usually polymerized on a surface to make a film. They can be deposited at room temperature by chemical vapor deposition [80].

The CVD discovery for Parylene was first reported by Szwarc in 1947 when he found a polymer as one of the products formed in the vacuum thermal decomposition (pyrolysis) of p-xylene [81]. However, the yields of polymer film were only a few percent even at very high pyrolysis temperature. It was not until 1966 when Gorham found a much more effective process starting with the vacuum pyrolysis of di-p-xylylene ([2.2]-p-cyclophane) [82].

Chemical Vapor deposition is carried out in a machine called parylene coater. The process has different steps and different operational settings. The CVD is a batch process where only a well-defined quantity of polymer is deposited per cycle.

The coater is divided in different units as follows:

- Vaporizer, where vaporization of the solid dimer takes place;
- Pyrolysis Furnace, where dimer Pyrolysis is carried out and monomer formation occurs;
- Deposition Chamber, where the deposition happens at room temperature.

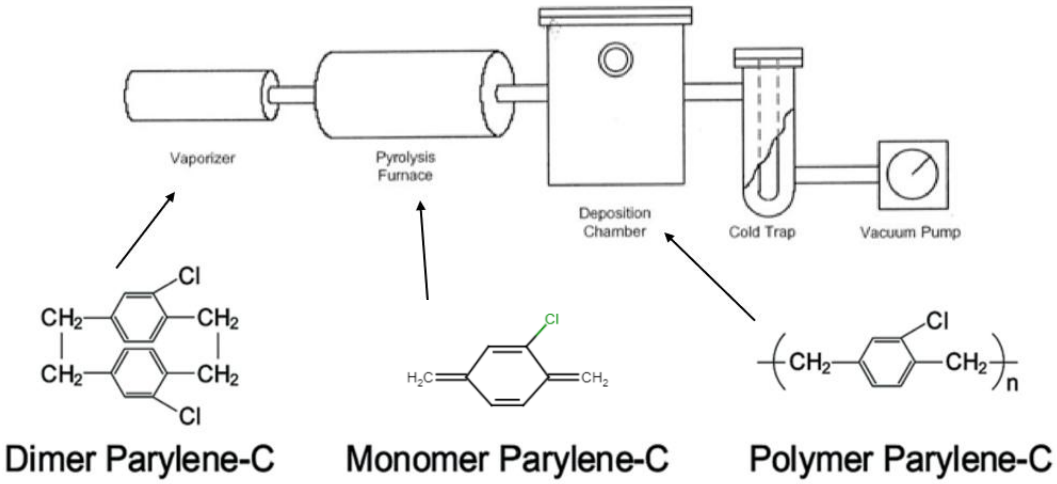

Figure 1.16: Reactions and operative scheme of a Parylene coater

All the entire system is kept under strong vacuum condition (around 20.8 mtorr) to favour polymerization.

The process starts with loading a precise amount of dimer in vaporizer. After that the vacuum pump is switched on to reach the target starting pressure. Once it is reached the vaporizer heat up until the vaporization temperature(around 140-150 °C). The vaporized dimer enter in Pyrolysis furnace, where the temperature is around 690 °C, and exit as a monomer. Once it reaches the deposition chamber it starts polymerizing on the surface (Figure 1.17).

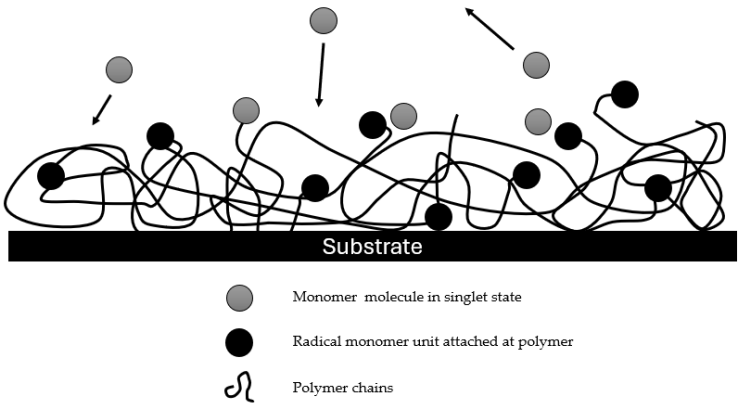

Figure 1.17: Surface polymerization for general parylene

The cooling trap is used to eliminate the excess of monomer that does not deposit, to prevent it from entering the vacuum pump.

The process is carried at a constant deposition pressure to ensure a constant deposition flux on the surface. The operation time is proportional to the amount of dimer that is loaded inside and also the thickness is strictly connected to this.

1.3.4.1. CVD optimization parameters

The parameter that affect the process are: substrate temperature, deposition pressure, amount of dimer loaded and deposition time.

The deposition time is strictly correlated with the amount of dimer loaded, increasing the amount of DPX-C extends the time the process will take to be completed. It is linearly connected to the deposited polymeric film thickness on the substrate.

Additionally, the deposition time is also dependent on the deposition pressure. Using a higher pressure means working with a more concentrated environment inside the chamber, which result in a faster deposition. However, a deposition that is too fast will result in films with lower homogeneity and can results in hazy, non-transparent film.

Furthermore changing the substrate temperature affects the deposition rate and film properties [75], [76], [83], [84], [85], [86], [87]. It shows an increase in deposition rate with a decrease in temperature as shown in Figure 1.18.

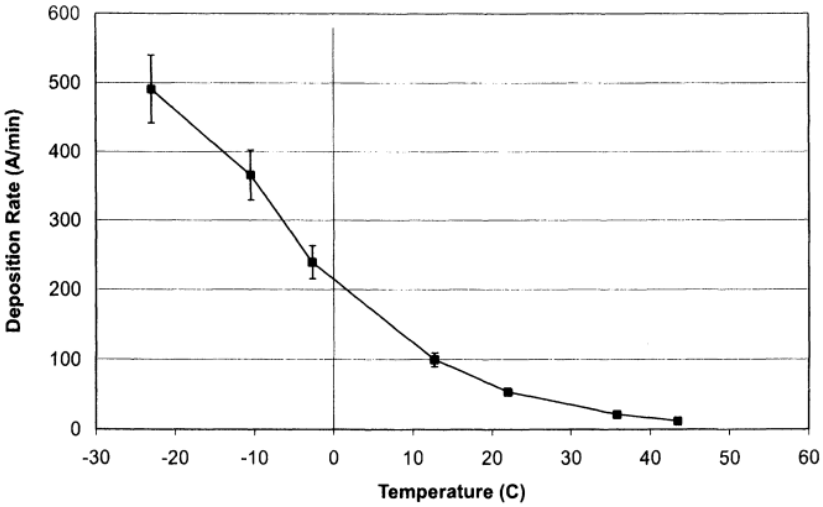

Figure 1.18: Deposition rate in function of temperature at pressure constant (4.0 mTorr) [80].

Usually, the substrate temperature does not control the mass transport which is ideally only controlled by transport of monomer into the system. However diffusion of reactants through a boundary layer is a temperature activated process and is proportional to T^2 [80]. Additionally, desorption is also a temperature activated process, which can further limit the polymerization rate.

The effect of pressure impacts mainly the reaction rate that is shown to be proportional to P^1, $P^{3/2}$ and P^2 for the most of deposition reactions [74], [75], [76], [83], [84], [85], [86], [87]. This general power law behaviour can be explained in terms of kinetic adsorption limited process. For Parylene at ambient temperature is shown to have a linear behaviour [80].

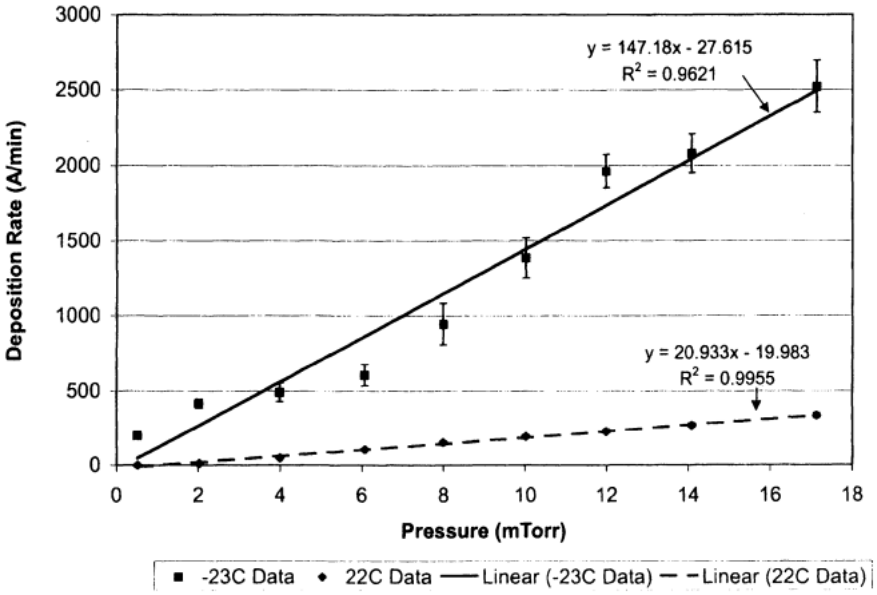

Figure 1.19: Deposition rate in function of pressure at two different fixed temperature [80]

From Figure 1.19 emerges that there is a minimum pressure below which no deposition occurs.

Since the CVD process is described as kinetically controlled deposition process [80], it can be described only considering the limiting step, the absorption process. For that reason a Chemisorption model has been chosen to fit the CVD process (for more detail refer to [80]).

1.3.5. Applications

Parylene is a versatile polymer widely utilized in various advanced applications due to its remarkable properties such as biocompatibility, chemical resistance, and dielectric strength.

In medical devices and implants, Parylene is employed in neuroprosthetic applications to create flexible neural interfaces that connect implantable electrode arrays, with external devices, providing both mechanical and electrical connectivity.

Parylene's application extends to microfluidics, where it is used in lab-on-a-chip devices for creating microvalves and microchannels, demonstrating its utility in handling biological samples and chemical reagents efficiently [88], [89], [90], [91], [92].

Furthermore, in biomedical coatings, Parylene-C is developed to produce super hydrophobic surfaces, which are particularly beneficial in reducing biofouling and enhancing the biocompatibility of medical implants.

Parylene's applications also span to space and electronics, where its properties are leveraged for creating durable and reliable coatings in harsh environments [93], [94], [95], [96], [97].

1.4. Aim of the Work

The rapid and precise tuning of lead-halide perovskite nanocrystals' (LHP-NCs) photoluminescence into the deep-blue spectral region remains a critical challenge for next-generation display and lighting technologies. This thesis addresses that challenge by developing a novel, gas–solid phase ion-exchange methodology which leverages chlorine released from parylene-C during chemical vapor deposition (CVD). In doing so, we seek not only to demonstrate a new synthetic route to pure-blue emitters but also to understand, and ultimately control, the mass-transport and reaction kinetics that govern halide exchange at the nanoscale.

Concretely, this work pursues four interlocking objectives:

1. Proof-of-Concept of Parylene-Driven Anion Exchange
    - Show that chlorine liberated from parylene-C coatings can effect a clean, reproducible Br→Cl exchange in $CsPbBr_3$ and MA/FA-mixed perovskite NC films, shifting emission from ~525 nm down to 460–480 nm (or below) without the need for liquid-phase reagents.
    - Quantify the maximum achievable blue-shift, the exchange depth profile (via XPS/TOF-SIMS), and any accompanying changes in crystallinity (XRD) or morphology (SEM/AFM).
2. Design and Optimization of a Mass-Transfer Control Device ("Flux Limiter")
    - Engineer a 3D-printed, multi-channel holder that constrains chlorine vapor diffusion to the NC layer, thus fine-tuning reaction rate and exchange extent.
    - Systematically vary channel length (30–70 mm), diameter (1–3 mm), and flow conditions to decouple diffusion-limited versus reaction-limited regimes.
    - Correlate device geometry with observed blueshift, PLQY retention (>50 %), and full-width at half-maximum (FWHM) narrowing.
3. Development of a Predictive, One-Dimensional Kinetic Model
    - Formulate and solve a finite-difference model coupling Fickian diffusion of Cl_2 through parylene with first-order surface reaction kinetics.

- Use experimental data (blueshift vs. channel length) to extract key parameters, exchange rate constant $K_{exchange}$, reaction order n, and effective diffusion coefficient D .
- Validate model predictions against independent test runs, aiming for <5 % deviation in predicted emission wavelength.

4. Mechanistic Elucidation of Gas–Solid Exchange Pathways
    - Combine steady-state and time-resolved photoluminescence (TRPL), photoluminescence quantum yield (PLQY), and UV–Vis absorbance to distinguish true Br→Cl exchange from degradation or etching artifacts.
    - Probe the role of native surface ligands (oleate/oleylammonium) in mediating halide flux using ligand-exchanged NCs and in situ IR spectroscopy.
    - Assess long-term stability (thermal, photochemical) of the blue-shifted films under ambient and inert conditions.

2 Methods

2.1. Materials used

Toluene (99.7% Sigma Aldrich), toluene dry (extra dry over molecular sieves 99.85% Sigma Aldrich), oleic acid (OLAc, 90% Sigma Aldrich), oleylamine (OLAm, 80-90% Thermo Scientific), octyl ammine (OA 99% Sigma Aldrich), lead bromide ($PbBr_2$, 98% Acros Organics), caesium carbonate (Cs_2CO_3, 99.9% trace metals basis Sigma Aldrich), caesium acetate ($CsCH_3COO$, 99% for analysis Acros Organics), methylammonium bromide (MABr, 98% Sigma Aldrich), formamidinium bromide (FABr, 98% Merk),guanidinium bromide (GABr, Aldrich), n-decylamine ($C_{10}H_{23}N$, 99% thermo scientific), N,N-dimethylformamide (DMF, extra dry over molecular sieves 99.8% Acros Organics), ethanol (EtOH, extra dry 99.85% Thermo Scientific), acetone (ACE, extra dry 99.8% thermos scientific), 1-octadecene (ODE, 90% Sigma Aldrich), ethyl acetate (EA, extra dry over molecular sieves 99.9% Thermo Scientific), hexane (extra dry over molecular sieves 97% Thermo Scientific), dichloro-p-cyclophane (DPX-C, Specialty Coating Systems), tri-n-octylphosphine oxide (TOPO, 99% Agros Organics). All chemicals were used as received. Cs_2CO_3, $MABr_2$ and $FABr_2$ were stored in a glovebox.

2.2. Synthesis of $CsPbBr_3$ Microwave (MW)

In a 30 ml reactor vessel equipped with a stirring bar, 19.9 mg of $CsCO_3$ (0.122 mmol Cs^+), 91.9 mg of $PbBr_2$ (0.250 mmol), and 333 mg of TOPO (0.861 mmol) are added. Subsequently, 10 ml of ODE, 666 µl of OA (2.11 mmol), and 666 µl of OAm (2.02 mmol) are also added. For synthesis, the vessel is placed in a microwave reactor, the temperature is set to 160°C, the heating time is set to 5 minutes, and the stirring speed is set to 600 RPM, with a hold time of 5 minutes and a cooling target of 55°C. For purification, 6.66 ml of hexane are added to the crude solution, briefly stirred, split into two centrifuge tubes, vortex mixed, and centrifuged at 8000 RPM for 8 minutes, with the supernatant discarded. The precipitate is redispersed by adding 3.33 ml of hexane to each tube, centrifuged at 5000 RPM for 5 minutes, the supernatant is collected, and it is filtered with a 0.2 µm Teflon filter into a 10 ml vial.

2.3. Synthesis of (MA/FA)$PbBr_3$

The precursor solutions are prepared as follows: 0.6 M PbBr2 by dissolving 0.881 g in 4 ml DMF, 0.6 M MABr by dissolving 0.269 g in 4 ml EtOH, and 0.6 M FABr by dissolving 0.300 g in 4 ml EtOH. For the synthesis, a magnetic stirrer is placed in a 100 ml round-bottom flask. The MABr and FABr precursor solutions are mixed together in equal parts, using 2 ml of each in a new vial. Into the round-bottom flask, 12.5 ml toluene is added as the solvent for QDs, followed by 625 µl oleic acid and 30 µl decylamine (or 50 µl of oleylamine if we want to use it as ligand) to dissolve the PbBr2. Then, 625 µl PbBr2 precursor solution is added dropwise, and if undissolved, it indicates too little amine or too much PbBr2. Following this, 625 µl FA/MABr precursor solution is added swiftly. After waiting for 1 minute, the solution is transferred to a 50 ml centrifuge tube, vortex mixed, and centrifuged at 10000 rpm for 8 minutes. The supernatant is discarded, 2 ml toluene is added to redisperse the precipitate, and the solution is centrifuged again at 8000 rpm for 8 minutes. A 5 ml syringe with a needle is used to draw the supernatant, which is then filtered using a 0.2 µm membrane filter PTFE and filled into a 5 ml vial.

2.4. Synthes of $CsPbBr_3$ with Hot Injection (HI)

Caesium lead bromide (CsPbBr3) NCs are synthesized by adapting the synthesis protocol described by Protesescu et al. 2015[1].

Dried OLAc and OLAm are obtained by placing 20 mL of OLAc or OLAm in a 50 mL 2-neck flask and drying under vacuum at 100°C for 1 hour. Caesium oleate (Cs-oleate) precursor is prepared by loading into a 50 mL 3-neck round-bottom flask equipped with a magnetic stirrer 15 mL of ODE, 306 mg of Cs2CO3, and 0.940 mL of dried OLAc. The mixture is then dried under vacuum for 1 hour at 100°C, and then heated under nitrogen to 120°C until all Cs2CO3 reacts with OLAc. Since Cs-oleate precipitates at room temperature, it is pre-heated to 140°C before injection. To synthesize the CsPbBr3 NCs, 10 mL of ODE and 110 mg of PbBr2 are loaded into a 50 mL 3-neck round-bottom flask equipped with a magnetic stirrer and dried under vacuum for 30 minutes at 100°C. The mixture is then placed under nitrogen and heated to 110°C, and 1 mL of dried OLAc and 1 mL of dried OLAm are added. Once PbBr2 is totally dissolved, the temperature is raised to 180°C and 1.6 mL of Cs-oleate is quickly injected. After 15 seconds, the mixture is cooled to room temperature using an ice-water bath. The reaction mixture is then distributed in 2 centrifuge tubes. The solids are precipitated by centrifugation at 10000 rpm (10600 x g) for 5 minutes, the supernatant is discarded, and the precipitate is redispersed in 0.6 mL (2 x 0.3 mL) of dry hexane using ultrasonication. The obtained suspension is centrifuged a second time under the same conditions. The supernatant contained in centrifuge tube is removed using a 5 ml syringe and is put in a vial adding 1.2 mL of hexane. The resulting liquid is mixed and is filtered. In that way a colloidally stable dispersion of NCs is obtained.

The synthesis has been scaled up 2 times and 4 times without significant differences being noticed in absorbance and photo luminescence quantum yield.

2.5. Parylene Coating

The parylene coater SCS PDS 2010 (Labcoater 2) has been used in this work not only as a deposition machine but also as a reactor environment when the exchange reaction could take place.

The parylene coating process consist in 3 main steps on the practical point of view. Heating system, DPX-C and sample loading, deposition step and clean step. Parylene coater is switched on and furnace heating is started with vacuuming to warm up the pump. Once the heating and sample preparation is done the pump will be warmed up (usually it takes around one hour). The system is than vented allowing the pressure to reach atmospheric value. At this point the sample are loaded and also the dimer is positioned inside an aluminium boat in the vaporizer. The system is brought to low vacuum pressure, 10.5 mtorr, before process starts. Deposition pressure can be changed according to have a higher or a lower deposition rate. Once the process is done the system is vented, the samples are removed and the Parylene coater is cleaned. The parylene film thickness dependency on the amount of DPX-C loaded is shown in Table 1.

Parylene film thickness	**DPX-C needed**
50 nm	100 mg
100 nm	200 mg
200 nm	400 mg
300 nm	600 mg
500 nm	1 g
1 µm	2 g
2 µm	4 g

Table 1: Amount of DPX-C loaded for a selected thickness of parylene film (linear behavior)

2.6. Sample preparation

The square glass samples are prepared with a thin film of perovskites. The substrates are first cleaned using various solutions in an ultrasonic bath. They are first immersed in a soap and water solution, then in plain water, followed by acetone, and finally in

isopropanol and sonicated for 20 minutes in each solution. After cleaning in the ultrasonic bath, the samples are dried with a N_2 gun and are cleaned with O_2 plasma cleaning step in order to activate the surface for the perovskites coating. The cleaned substrates are coated with lead halide perovskites via spin coating to achieve a clean and uniform film. The parameters used for 1 cm^2 sample were 2500 rpm, 400 for the acceleration, 50 seconds and 50µL of LHPs solution. The nanocrystals used are MAFA-based and Cs-based perovskites. Following preparation, the samples undergo a parylene deposition process to induce the blueshift. The film samples on glass substrates are evaluated by photoluminescence quantum yield (PLQY), while the silicon wafers, as substrates, are employed for X-ray diffraction (XRD), scanning electron microscopy (SEM), and profilometry measurements. The cleaning procedure was consistent across all samples.

2.7. PLQY

Luminescent materials convert the excitation energy into photons, usually this conversion doesn't have 100% efficiency due to various losses. To measure the conversion efficiency the quantum yield has been introduced [98].

The photoluminescence quantum yield (PLQY, η_{PL}) of a material is the ration between the number of photons emitted N_{em} and the number of photons absorbed N_{abs} (**2.1**).

$$\eta_{PL}(\lambda) = \frac{N_{em}}{N_{abs}} \qquad \textbf{2.1}$$

PLQY can also be seen as a measurement of the competition between radiative k_r and non-radiative k_{nr} processes in the material after the excitation (**2.2**).

$$\eta_{PL}(\lambda) = \frac{k_r}{k_r + \sum k_{nr}} \qquad \textbf{2.2}$$

The absolute η_{PL} was determined using the Quantaurus QY (C11347-11) from Hamamatsu equipped with 150 W Xenon light source and 3.3 inches integrating sphere, which is coated with highly reflective Spectralon. The η_{PL} of all samples were characterized at fixed the excitation wavelengths (λ_{ext}) of 370 nm.

2.8. XRD

X-ray diffraction (XRD) is a technique used to study the crystalline structure of materials. It works by directing a beam of X-rays at a crystal, where the X-rays interact with the crystal's atomic planes. According to Bragg's law (equation 2.3) constructive

interference occurs when the path difference between X-rays scattered by successive crystal planes equals an integer multiple of the X-ray wavelength (λ).

$$n\lambda = 2dsin\theta \quad \textbf{2.3}$$

Here, n is the order of reflection, d is the interplanar spacing, and θ is the angle of incidence. The diffraction pattern, consisting of the angles (θ) and intensities of these diffracted X-rays, is recorded. The correlation between theta and d is shown in Figure 2.1, where hkl are two parallel crystal planes.

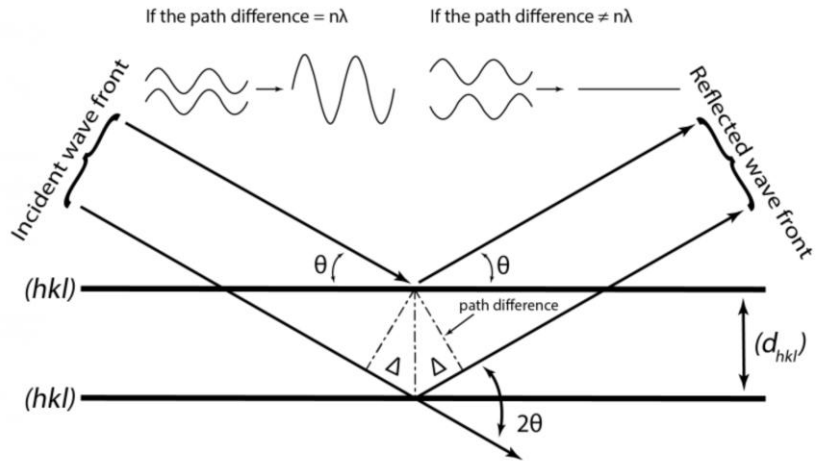

Figure 2.1: Diffraction scheme between two general planes (hkl) [99]

By analysing the positions and intensities of the resulting peaks, the crystal structure can be deduced, revealing details such as the size and shape of the unit cell and the arrangement of atoms within it. The measured was determined using X'Pert PRO-MDP from PAN analytical (DY2892).

2.9. UV-Vis Spectrometer

UV-Vis spectroscopy is an analytical technique used to measure the absorbance of ultraviolet (UV) and visible (Vis) light by a sample. When a sample is exposed to light in the UV-Vis range (typically 200-800 nm), molecules within the sample can absorb light at specific wavelengths, leading to electronic transitions.

According to Lambert-Beer Law the absorbance is a function of the wavelength resulting in an absorption spectrum that displays characteristic peaks corresponding to different electronic transitions.

$$A = \varepsilon cl \quad \textbf{2.4}$$

Where A is the absorbance, ε is the molar absorptivity coefficient and l is the path length.

By analysing these absorption peaks and performing calibration steps, it is possible to determine the concentration of the absorbing species. In the case of this work the instrument Jasco V-770 (D102661801) was used to prove the effectiveness of the ion exchange reaction.

2.10. Profilometer

Polymer films thickness was measured using a Bruker DektakXT surface step profilometer. The thickness was measured at the edge of a step created in the polymer film and measuring the difference in height between the polymer film and the silicon wafer.

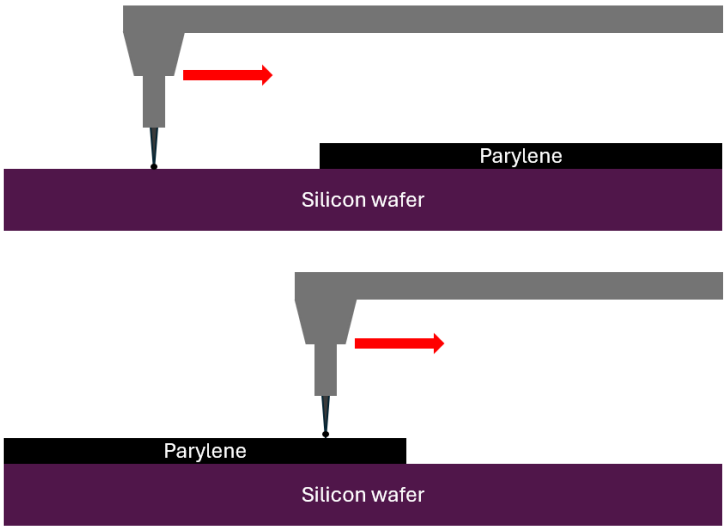

Figure 2.2: Profilometer film scanning from Substrate to Polymer and vice versa

Figure 2.2 represents the usual measurement procedure for a thin film of parylene. The scan is done in both direction in order to evaluate the best result.

3 Results and Discussion

3.1. Gas-Solid Ion Exchange through Parylene

Parylene C dimer, as shown in Figure 1.13, has in its structure a Cl group and for that reason can be a resource for a halogen exchange to modulate the emission colour of LHP-NCs. As described in chapter 1.2.2.1 the exchange between iodine and chlorine is hard to obtain. For this reason the attention has been focused on the exchange with bromine. The nanocrystals that have been used are $CsPbBr_3$, synthesised hot injection and microwave irradiation, and (MA/FA)$PbBr_3$ (with n-decylamine instead of oleylamine) obtained by LARP synthesis.

The reaction is carried inside a Parylene coater machine (see chapter 1.3.3 and 1.3.4 for more information), which is normally used for Parylene-C deposition purposes. Different NCs have been used to see the effect that parylene-C CVD has on different perovskites. Since it contains chlorine groups a possible exchange between halogens could happen.

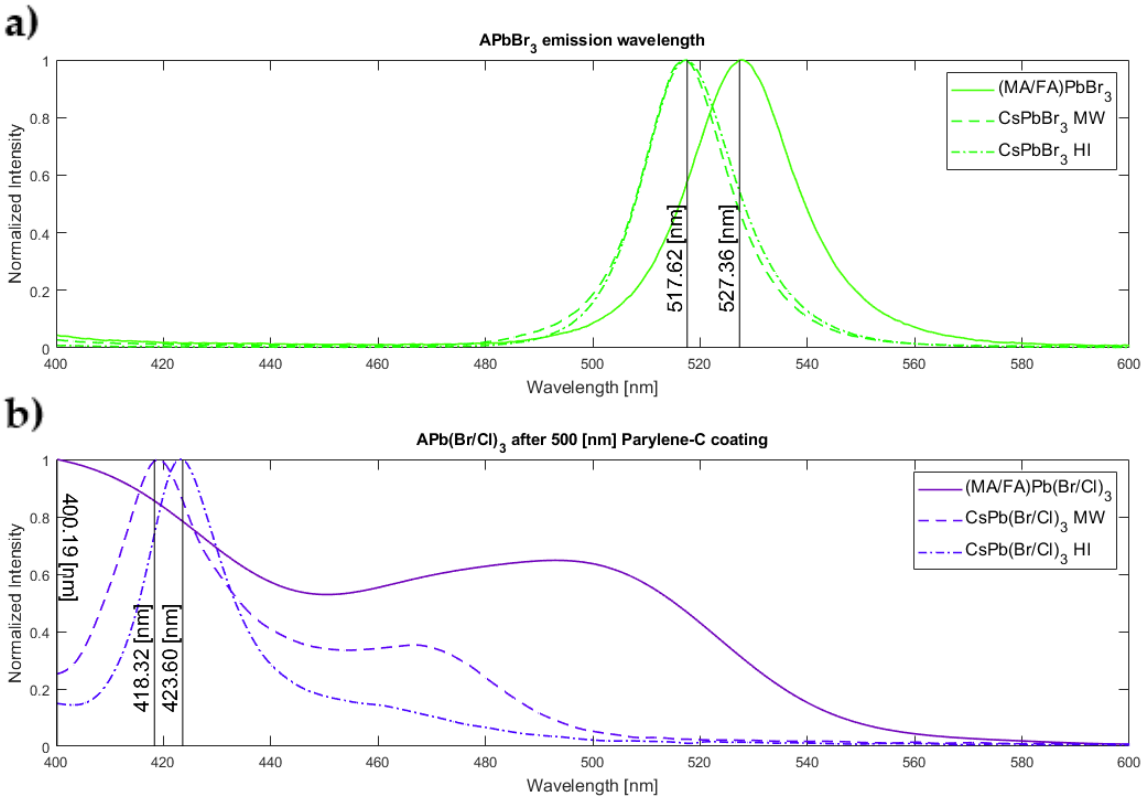

Figure 3.1: a) Reference wavelength peaks for the different LHPs NCs used; b) Shift in emitted wavelength due to ion exchange reaction with Parylene-C.

It can be seen from the graph above that an ion exchange reaction occurred due to the change in wavelength emission (see paragraph 1). The broad peaks, presented in Figure 3.1 b), are due to an inhomogeneity of the perovskite film thickness, resulting from LHP deposition by spin coating. Due to the geometry of the substrate more material gathers at the corner during the spinning step, leading to an increased thickness at the corners as seen in Figure 3.2. The thicker corners show a decreased blueshifting due to the ratio of chlorine that diffuses inside the NCs film.

Figure 3.2: Aspect of a sample after deposition of Parylene. On the corner the color is less blueshift due to the lower ratio between bromide and chlorine ions.

Keeping this phenomenon in mind the possibility to obtain a pure blue color (467 nm) using this new anion exchange technique was investigated. As a first step, the influence of the amount of deposited parylene on the degree of blueshifting has been evaluated.

The evaluation has been done using 25, 50,100, 200, 300, 400, 500 and 1000 nm deposited parylene. Increasing the thickness of polymer an increase in the Cl concentration of the NCs is expected and therefore stronger blueshift. Since the $CsPbBr_3$ obtained with microwave synthesis (Cs MW) and $CsPbBr_3$ obtained by hot injection synthesis (Cs HI) experience a similar behavior, as reported in Figure 3.1 a), has been investigated only Cs produced through micro wave synthesis. Additionally, MA/FA$PbBr_3$ with n-decylamine and oleic acid as ligands has been investigated, as this composition is commonly used for future LEDs applications [103].

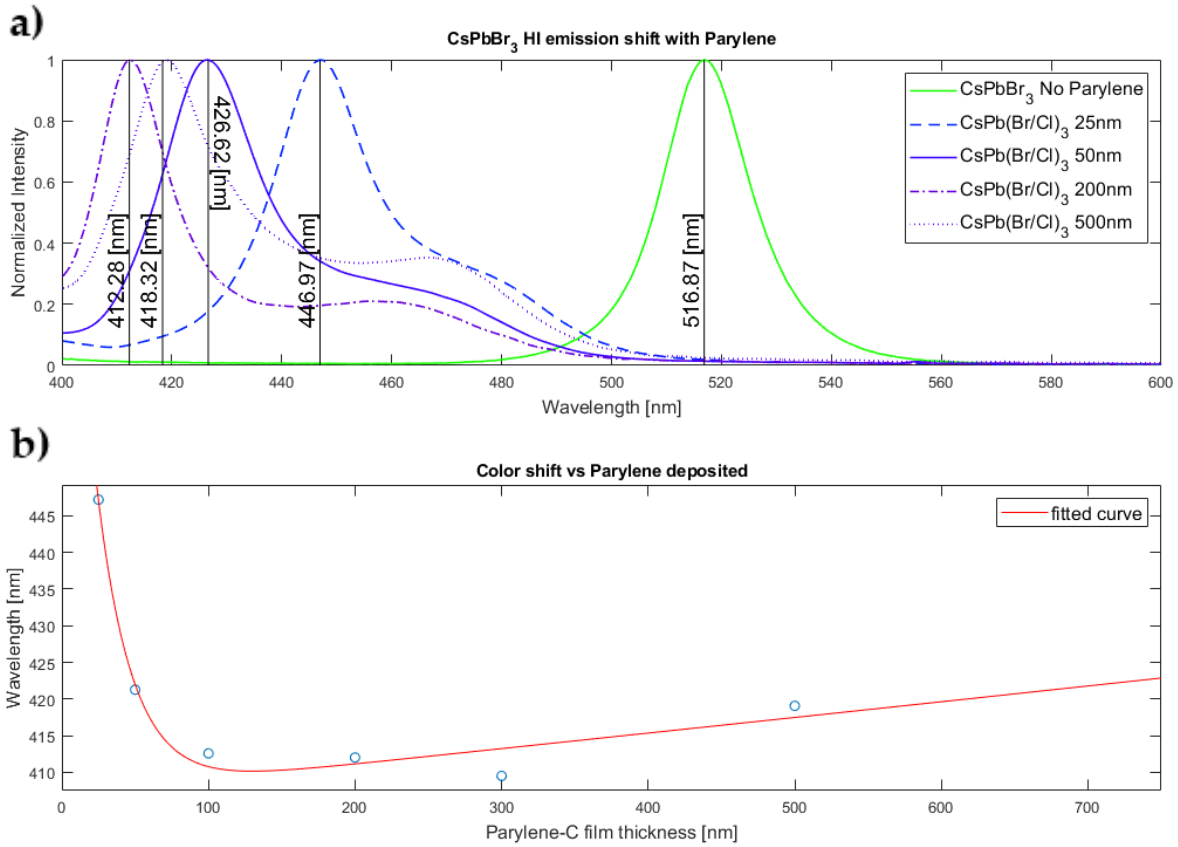

Figure 3.3: $CsPbBr_3$ wavelength shift according to deposited thickness of Parylene-C

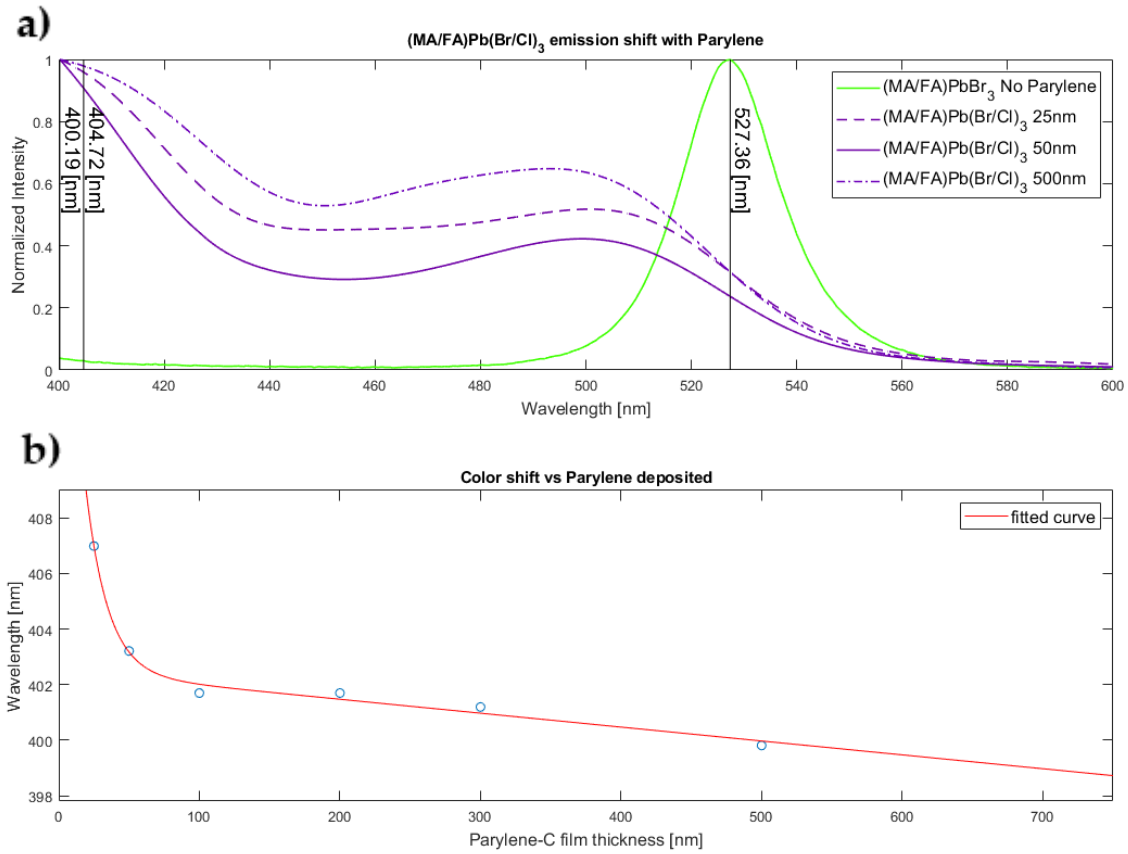

Figure 3.4: MAFA Perovskite wavelength shift according to deposited thickness of Parylene-C

As expected the blueshift increases with greater Parylene-C thickness. MAFA emerged to be more sensitive to the process. It reached rapidly an extreme blueshift, also with low quantity of Parylene. It also shows a degradation, with a decrease in PLQY and absorbance (near to 10 percent). Cs instead is more stable than the organic-inorganic counter-part, as it maintains the original shape of the emission peaks. The higher degree of shift in MAFA can be also explained due to the different film thickness of perovskite that is deposited on the substrate. The thicker the film deposited on the substrate and the higher will be the quantity of Cl necessary to reach a given value of blueshifting. This is strictly connected to the difference in viscosity or concentration between the two NCs solutions used for spin coating. Cs, has a lower solvent vaporization speed if compared with MAFA. This, coupled with higher concentration of NCs in solution contribute to a lower blueshift than MAFA.

The trend curves represent in Figure 3.3 b) and Figure 3.4 b) have a different behaviour starting from 300nm. Initially the decrease is evident in both the different NCs but toward higher film thickness the Cs-based samples show a deviation from the MAFA-based samples.

Observing the trend of Figure 3.3 b) and Figure 3.4 b), it became clear that altering only the amount of Parylene was insufficient to achieve a controllable and tunable blueshift.

The minimum usable and valid value for the parameters of the Parylene coater is 25 nm. For coating below this value the film appears to be heterogenous and the process became difficult to control in terms of reaction conversion and reproducibility.

The deposition of a 50 nm film is used as starting point for the optimization. The idea is than to change the deposition parameter (see chapter 1.3.4.1) or transform the process in such a way that the process moves from a kinetically limited regime to a mass transfer limited regime in order to achieve higher control over the blueshift and obtain pure blue emission.

3.2. Diffusion Limitation Solution

To enable a precise control of the blueshifting through mass transfer an additional resistance of mass transfer has been used. The idea was to mask the sample creating some new pathways where the reactive species had an increased difficulty to reach the sample.

The idea was to develop an assembly encasing the sample to decrease the flux that goes into contact with the samples, which subsequently will be referred to as "flux limiter". Thinking about atmospheric systems a new resistance can be added using, for instance, a small channel (Figure 3.5). This way the diffusion plays a very important role and it becomes the rate limiting step, enabling a greater control of the reaction. If the channels are small and long to create enough resistance to mass transport the reaction conversion, as a consequence, will be decreased.

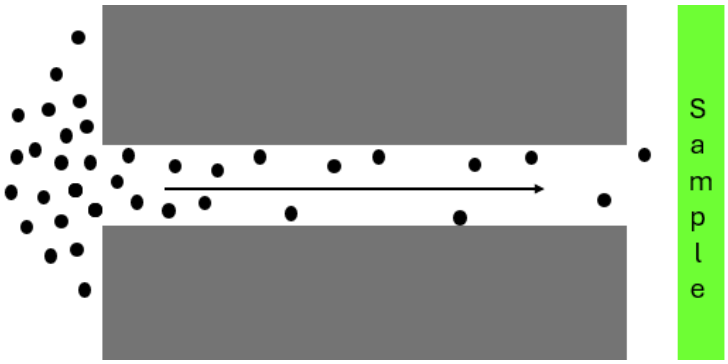

Figure 3.5: Illustration of regular diffusion into a narrow channel in an atmospheric system

The concept of diffusion limitation is strictly correlated to the diffusion coefficient of gas species that is a function of temperature and pressure of the system. The parylene coater system is far from being an atmospheric pressure system. The system operates under medium vacuum pressure, not atmospheric pressure, and so the explanation must be integrated with a deposition process. In this vacuum environment, diffusion plays a dominant role in transport phenomena. It's important to note that the mass transport limitation in this process is due not only to diffusion constraints but also to the rapid deposition of parylene on the walls. As a result, the combination of diffusion

and channel deposition leads to a greater-than-expected diffusion limitation (Figure 3.6).

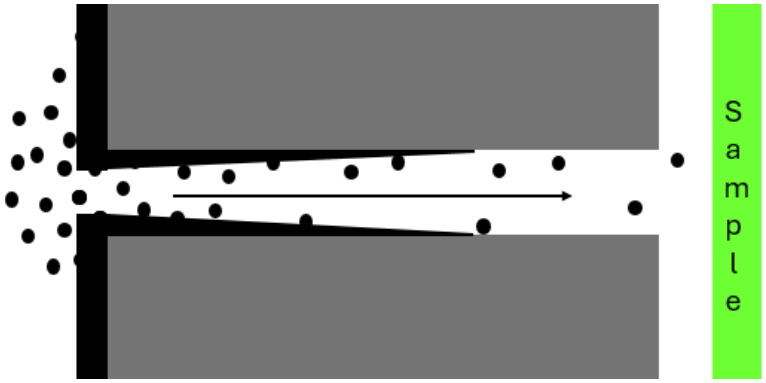

Figure 3.6: Mass transport limitation coupling the two phenomena: deposition and diffusion inside a tube. The black regions show the partes where the polymer film is growing.

These are concepts that guided the modelling of the flux limiter.

It has been created using the software Fusion 360 and it has been printed with a 3D printer, Bambu Labs X1 Carbon Combo. ABS was used as the printing material.

Figure 3.7: 3D models of the flux limiter with 4 channels of 60 mm length. The holder is designed for 1 cm^2 substrates

The flux limiter (FL) presented in Figure 3.7 is designed to decrease the flux of the reactive species. The sample is positioned inside the holder and the upper part, where channels are present, is screwed on. Just above the sample position a small chamber ensures the incoming reactive species is evenly distributed to keep the reaction as homogeneous as possible

Different types of FL have been created but the one presented is the one that was found to work the best to achieve pure blue emission, given the geometrical constraints of the deposition chamber. The screw-on enclosure reduces significantly the leaks and create a better control and homogeneity inside the sample camera.

This shape has been chosen to be as simple as possible for 3D printing in order to obtain a high quality print, without significant defects and distortions.

The design parameters of the FL are: channel diameter, channel length, number of channels and the dimension of the substrate. By adjusting these parameters it is possible to achieve complete control of the perovskite conversion and therefore the degree of shifting in the blue region of the visible spectrum.

The following optimization has been performed choosing a substrate dimension of 1 cm^2, a channel number of 4 and a diameter has been chosen as 3 mm initially for Cs.

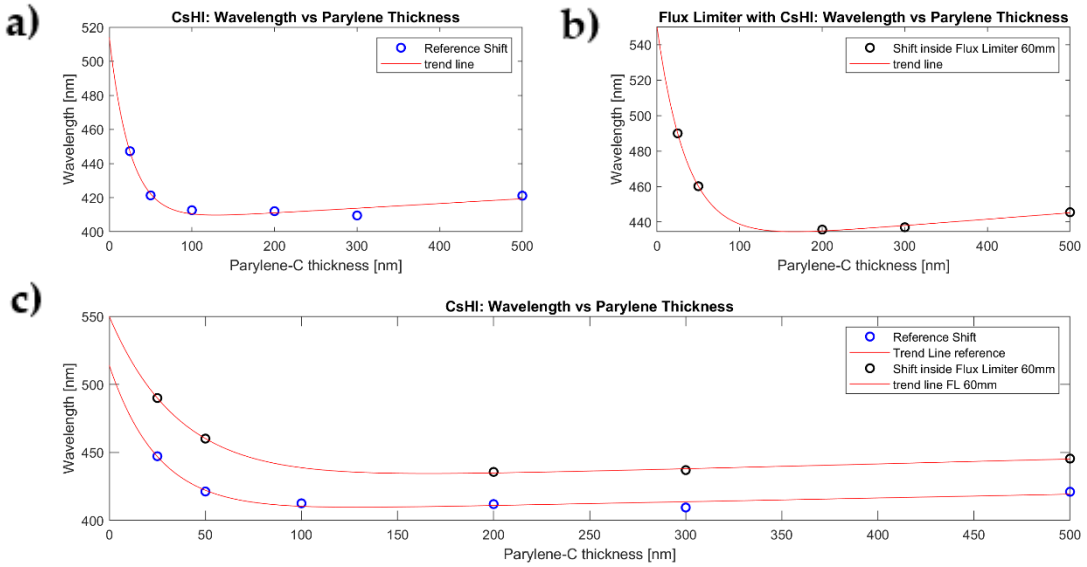

Figure 3.8: Experimental data fitting of $CsPbBr_3$ HI in a) outside flux limiter, b) inside flux limiter and c) comparison between the two. Blue dots represent the exchange reaction without using FL. Black dots instead represent the reaction using flux limiter with 4 channel with 60 mm length and 3 mm diameter. The solid red curves are interpolation fits drawn to guide the eye and highlight the overall trend of the wavelength shift as a function of Parylene-C thickness.

In Figure 3.8 c) the difference between no FL and the use of the FL is shown and the film emission was measured by a PLQY machine (370 nm excitation wavelength). The channel length was chosen to be 60mm. As can be seen from the two trend curves the use of a mass transfer limiting system permits to add a limiting barrier to the reaction for each film thickness of deposited Parylene. The curves are not monotonous decreasing because the liquid solution used had different absorbance. Difference in absorbance arises from a difference in solution concentrations used during sample preparation. The higher concentration of the NCs solution causes an increase in perovskites film thickness. The thicker the film the more chlorine ions are needed to obtain a blueshift closer to the target one. The film used showed an absorbance around 0.22 and 0.28.

Cs HI	Parylene-C film thickness [nm]			
	25	**50**	**200**	**500**
Normal exchange reaction wavelength	447.2233 [nm]	421.285 [nm]	412.0267 [nm]	421.0867 [nm]
Wavelength obtained by exchange reaction using FL 60mm with 2mm diameter	490 [nm]	460.15 [nm]	435.67 [nm]	437 [nm]

Table 2: Blueshift obtained according to the parylene film thickness deposited on a Cs HI samples.

The limiting effect is useful to reduce the reaction conversion. The effect of the channel length has been also studied and is presented in Figure 3.9.

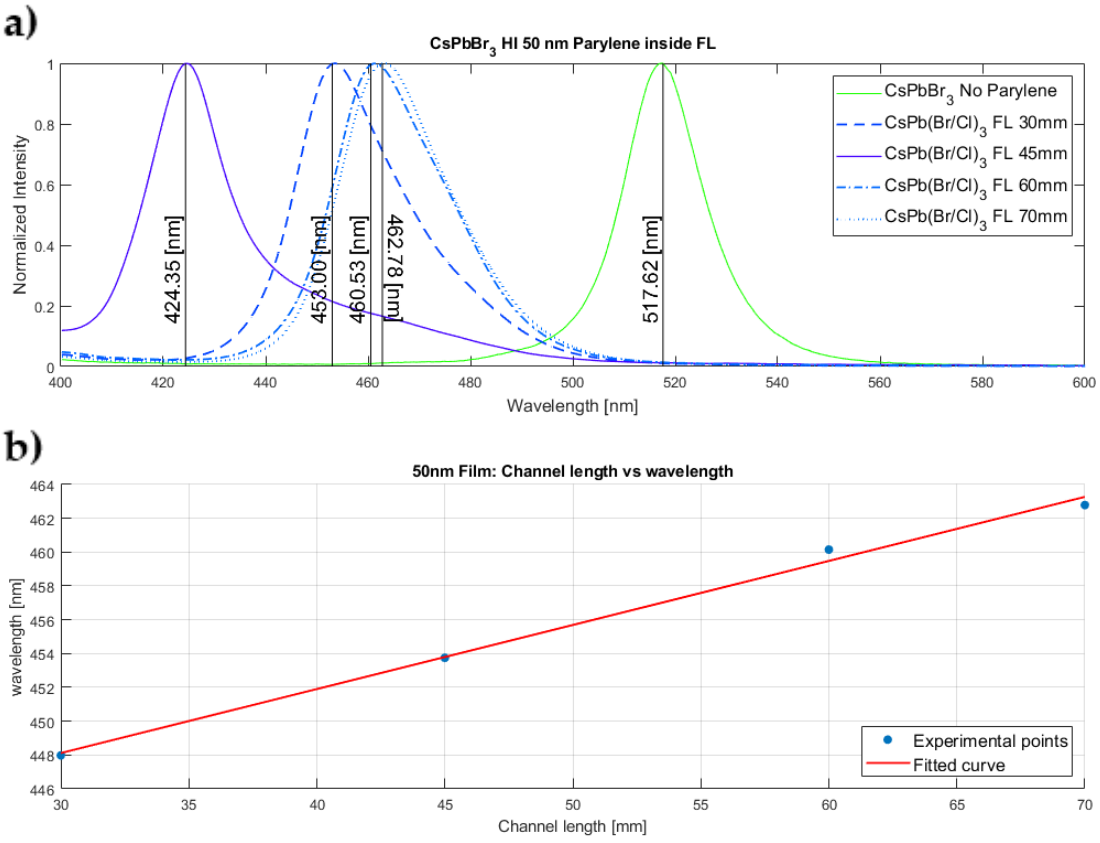

Figure 3.9: Reaction conversion with respect to channel length. The only parameter changed in the FL was channel length. The diameter and substrate dimension were kept constant

respectively to 3mm and 1 cm^2. a) Normalized peaks obtained for different FL; b) Linear regression between wavelength and channel length.

As can be expected increasing the channel length creates a more effective barrier to the diffusion of the reactant resulting in a reduced blueshift. Increasing the channel length increases also the surface area. This means that the decrease in conversion is not only achieved due to diffusion limitation but also thanks to the increase in deposition area, meaning that more parylene deposited on the wall before reaching the sample surface.

Since the length of 60 mm was not enough for reaching pure blue target that is around 467-470 nm the channel diameter has been decreased. The effect of the decrease should favor the diffusion limitation inside the channel but also should decrease the total area of the channel. A decrease in area should decrease the total area where the polymer can deposit but should also decrease the flux of reactive species inside each channel.

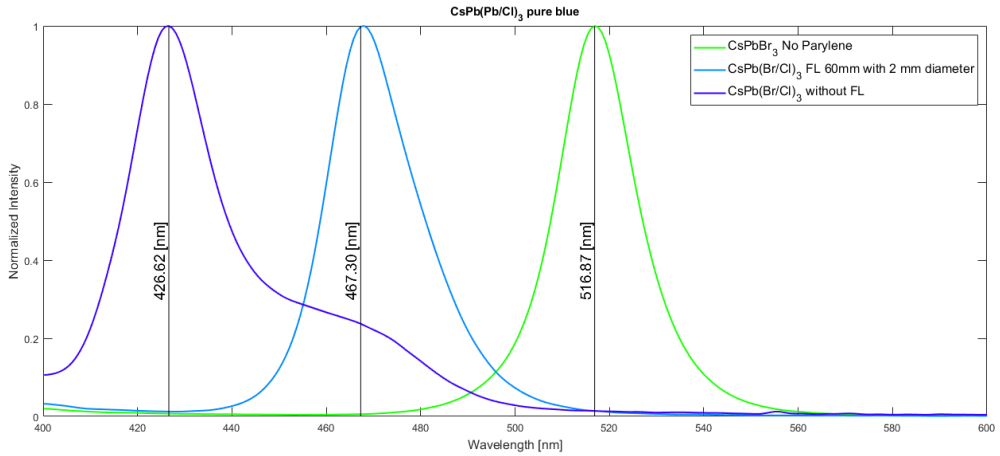

Figure 3.10: Pure blue ion exchanged obtained using Flux Limiter with 4 channels with length 60mm and 2 mm diameter.

As shown in Figure 3.10 the reduction of the channel diameter reduces the amount of reactant reaching the sample, resulting in a smaller blueshift. It means that the flux reduction has a more important role than the decrease in deposition area. It can also be explained considering that the side area decreases linearly with diameter, while the flux has a second power decrease (since the cross sectional area depends on the diameter by power of two).

The shifted peaks are a bit wider than the reference due to the coating inhomogeneities of the square substrate (as explained in chapter 3.1).

The value of absorbance and PLQY are reported in the Table 3.

Cs HI	Quantum Yield	Absorbance	Peak Wavelength
Reference sample without parylene deposited	0.645	0.3257	516.87 [nm]
Reacted sample inside FL	0.4867	0.2783	467.30 [nm]
Reacted sample without FL effect	0.2393	0.270	426.62 [nm]

Table 3: PLQY, Absorbance and wavelength of pure $CsPbBr_3$, a sample reacted inside FL (60mm and 2 mm diameter) and one without the limitation.

The PLQY decrease with conversion (with the amount of chlorine that is exchanged) because of the creation of new trap states. Chlorine atoms induce the shift of conduction band and additional trap states originating from unpassivated PbCl6-X octahedra, creating new not emitting pathways. The new trap states decrease the amount of excited electron relaxation by radiation and therefore decrease the PLQY. Another phenomenon that has been observed, the effect of vacuum on LHP-NCs. Strong vacuum or long exposure to vacuums pressure affects the PLQY. Placing a film of NCs under medium vacuum condition for an extended period of time, as the one used in parylene coater, can provoke a degradation of the film. This means that a further optimization is ensuring a reduction in reaction time to prevent of this phenomenon. This degradation is shown in more detail in appendix A.

The same optimization has been carried also for MA/FA-based NCs with the purpose of LEDs applications. This NCs are better for devices application due to the shorter ligands used in the synthesis. Shorter ligands means less resistance for electron flow.

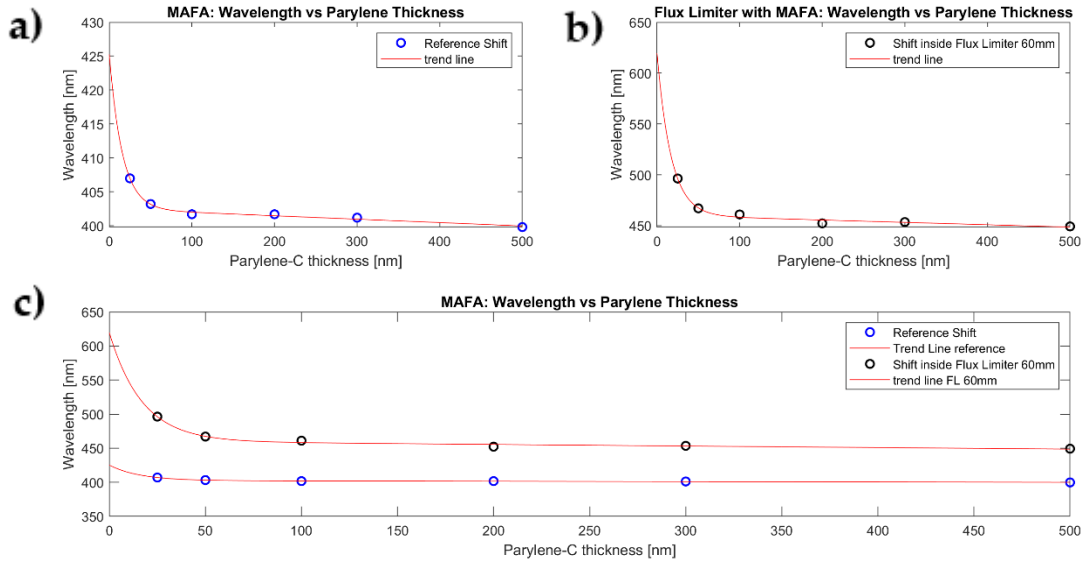

Figure 3.11: Experimental data fitting of (MA/FA)$PbBr_3$ in a) outside flux limiter, b) inside flux limiter and c) comparison between the two. Blue dots represent the exchange reaction without using FL. Black dots instead represent the reaction using flux limiter with 4 channel with 60 mm length and 3 mm diameter. The solid red curves are interpolation fits drawn to guide the eye and highlight the overall trend of the wavelength shift as a function of Parylene-C thickness.

(MA/FA)$PbBr_3$ has been found to be more sensitive to the reaction as shown in Figure 3.11. The parylene film thickness, above 50nm, does not influence to much the conversion of the reaction. It appears to be more degradable due to the thinner perovskites film deposited on the substrate. Due to this the effect of diffusion limitation is more important. The implementation of a diffusion limitation can prevent complete degradation of the NCs as shown in Figure 3.11 (looking at wavelength values).

MA/FA	**Parylene-C film thickness [nm]**			
	25	**50**	**200**	**500**
Normal exchange reaction wavelength	406.99 [nm]	403.2133 [nm]	401.7 [nm]	399.81 [nm]
Wavelength obtained by exchange reaction using FL 60mm with 2mm diameter	496.36 [nm]	467.047 [nm]	452.25 [nm]	449.233 [nm]

Table 4: blueshift obtained according to the parylene film thickness deposited on a MAFA-based samples.

Since the diameter necessary to achieve pure blue emission with Cs HI was 2mm, MA/FA-based samples, synthesized by LARP synthesis, have been directly optimized with the same diameter.

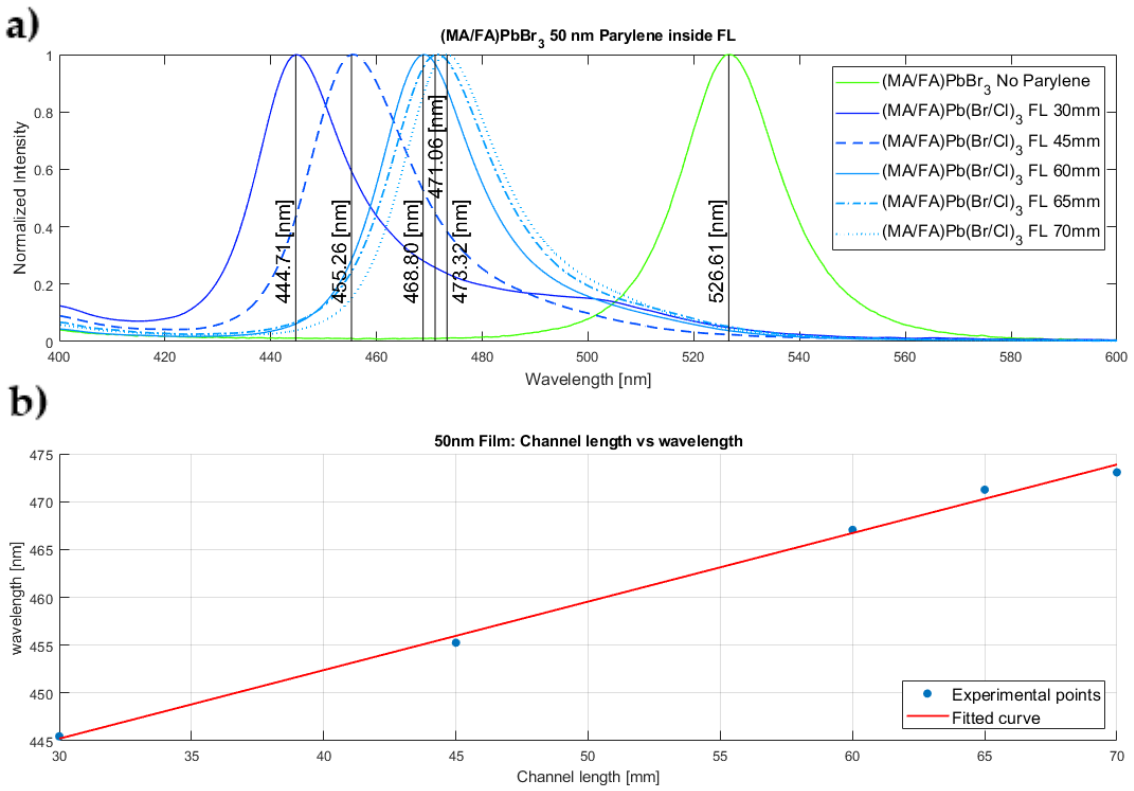

Figure 3.12: Reaction conversion with respect to channel length. The only parameter changed in the FL was channel length. The diameter and substrate dimension were kept constant respectively to 2mm and 1 cm^2. a) normalized peaks for different FL used; b) linear regression between wavelength and channel length.

The behavior is strictly similar to the one seen in Cs HI with the only difference that is strongly more susceptible to the reaction in normal condition without using FL. Also in that case the fitted curve is linear because it does not depend on the exchange kinetics but only on the diffusion system. Since that the current version of FL did not change, the trend is linear as before.

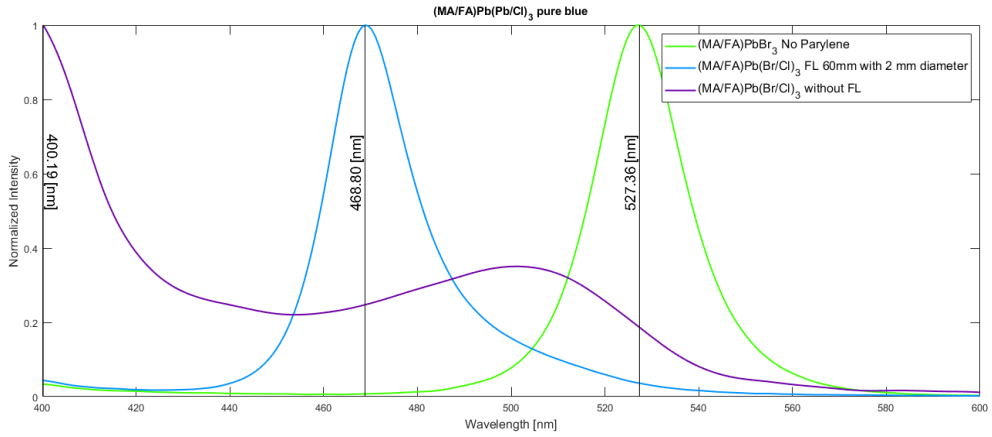

Figure 3.13: Pure blue ion exchanged obtained using Flux Limiter with 4 channels with length 60mm and 2 mm diameter.

The best results for pure blue is shown in Figure 3.13. The case of reaction without the Flux Limiter has a strange behaviour with respect to the other two. This trend is due to the degradation of the perovskites, the effect of the normalization accentuate the double peaks nature of the emission spectrum. The LHPs synthetized with LARP appear to be a bit wider than the Cs HI, which is commonly known for organic-inorganic LHP NCs. The effect of the exchange increase the broadness of the peak manly because of the difference in thickness between the corner and the centre of the sample (see Figure 3.2).

MA/FA	**Quantum Yield**	**Absorbance**	**Peak Wavelength**
Reference sample without parylene deposited	0.749	0.2273	527.36 [nm]
Reacted sample inside FL	0.566	0.2213	468.80 [nm]
Reacted sample without FL effect	0.07567	0.158	400.19 [nm]

Table 5: PLQY, Absorbance and wavelength of pure (MA/FA)$PbBr_3$, sample reacted inside FL (60mm and 2 mm diameter) and without the limitation.

The results presented in Table 5 are considered as a good starting point for the fabrication of blue devices. The limiting phenomena create a strong barrier effect to degradation and permits to use these ion-exchanged NCs for device fabrication.

3.3. Numerical Prediction Model

A numerical model has been developed to predict the behaviour of the sample wavelength after deposition process. To realize the model it is necessary to use the

experimental data to find the ion exchange kinetics. However it was not the only reaction that had to be evaluated. It is also necessary to take into account the deposition monomer on the channel wall. This deposition reaction has been modelled as a material flux from the centre of the channel to the wall.

$$K_{avg}(C - C_{wall}) \quad \textbf{3.1}$$

Where K_{avg} is an average mass transfer coefficient for the channel length and C_{wall} is the concentration of the reactive species at the wall.

The model requires some assumptions:

- Convective velocity is set equal to zero because the process is purely diffusive inside the channels. It can have only an effect outside the flux limiter;
- 1D model: This may be a good approximation due to the high value of diffusion coefficient in the vacuum condition (operating pressure equal to 20.8 mtorr);
- The ion exchange reaction is only present at the end of the channel, since is the only part in contact with the sample;
- Sample is in direct contact with the end of the channel.

Temperature and pressure are constant for the entire reaction time.

The model provides the concentration along the channel in time and the final wavelength that the sample will have. Since the wavelength is correlated to the final ratio between chlorine and bromine ions the following formula has been used:

$$\lambda = \frac{C_{Cl}}{C_{Br}}\left(\lambda_{ref,Cl} - \lambda_{ref,Br}\right) + \lambda_{ref,Br} \quad \textbf{3.2}$$

Where C_{Cl} and C_{Br} are respectively the molar concentration of chlorine and bromine inside the sample, $\lambda_{ref,\,Cl}$ and $\lambda_{ref,\,Br}$ are the reference wavelength for the $CsPbCl_3$ and $CsPbBr_3$ (410 and 517 nm).

The final concentration of chlorine that is present in the sample has been evaluated considering two models. The first one that accounts only for the diffusion and the deposition reaction on the channel walls and the second that accounts also for the ion exchange reaction with the sample. To enable the wavelength evaluation, C_{Cl} is calculated as the difference between the integral of the concentration at the end of the channel in time using the model without the ion exchange reaction and the one that consider also it.

$$C_{Cl} = \int_0^t C_{noRxn}(t, L)\, dt - \int_0^t C_{Rxn}(t, L) dt \quad \textbf{3.3}$$

Where t is the time and L is the length of the channel.

The two models differ only for the evaluation in the final point of the channel. The model that presents the ionic exchange is given by equation 3.4:

The system was governed by the following PDE:

$$\frac{\partial C}{\partial t} = D\frac{\partial^2 C}{\partial z^2} - \frac{4K_{avg}}{d}(C - C_{wall}) \quad \textbf{3.4}$$

Together with the following boundary conditions:

$$C(z, t = 0) = C_0(z) \quad \textbf{3.4a}$$

$$D\frac{\partial^2 C}{\partial z^2}\bigg|_{z=L} = K_{exchange}C(z = L, t)^n \quad \textbf{3.4b}$$

$$C(z = 0, t) = C_F(t) \quad \textbf{3.4c}$$

where z is the axial coordinate, t is time, C_F is the feeding concentration, D is the diffusion coefficient, d is the diameter of the channel, L is the total channel length, $K_{exchange}$ is the kinetic constant for the ion exchange reaction, n is the reaction order and C_{wall} is the concentration of reactive species at the wall. K_{avg} is the average mass transfer coefficient, which is the average of each local mass transfer coefficient at each point of the channel.

The model for the case without reaction is the same as before, the only difference stays in the z=L boundary condition where, instead of equation 3.4b, we have the equation 3.5.

$$D\frac{\partial C}{\partial z}\bigg|_{z=L} = 0 \quad \textbf{3.5}$$

The K_{avg} can be coupled with the constant and becomes K' that has a meaning closer to a reaction kinetic constant, as it is shown in equation 3.6.

$$K' = \frac{4K_{avg}}{d} \quad \textbf{3.6}$$

The model was created in MATLAB using finite difference method (FDM) with appropriate boundary conditions (BCs).

The diffusion coefficient for parylene-C monomer has been evaluated using the Fuller, Schettler, Giddings empirical correlation (1966).

$$D = 1e^{-3}\frac{T^{1.75}\left(1/\widetilde{M}_1 - 1/\widetilde{M}_2\right)^{1/2}}{p[(\sum_i V_{i1})^{1/3} + (\sum_i V_{i2})^{1/3}]^2} \quad \textbf{3.7}$$

Where p is the pressure in atmosphere, T is the temperature in K, V_{ij} are the volume of the molecule j and $\widetilde{M}_j$ are the molecular weights (N_2 and monomer). The diffusion coefficient evaluated with this formula is given in cm^2/s and is in the order of 4.5 10^3 cm^2/s. It appears to be quite high due to the very low pressure that is used during the process.

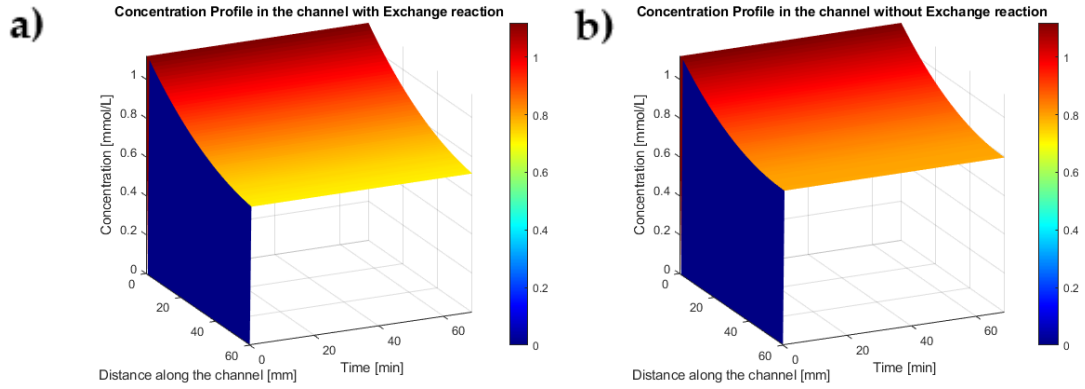

Figure 3.14: 3D plots of Concentration profile in function of time and channel length. a) Concentration profile with the gas-solid exchange reaction; b) Concentration profile without gas-solid exchange reaction.

The Figure 3.14 represents the evolution of the profile in time. As evaluated from Fuller equation the diffusion coefficient is huge compered to atmospheric one. This phenomena force the system to immediately reach the steady state condition due to the instantaneous diffusion inside.

The K' has been evaluated by fitting the experimental results, in terms of wavelength, with the model. In this way has been possible to obtain a K' that contains the K_{avg}. The deposited thickness, for fitting, has been set to 50 nm. The FL used presented 4 channels, with d=2mm, and different lengths as 30,45,60 and 70 mm.

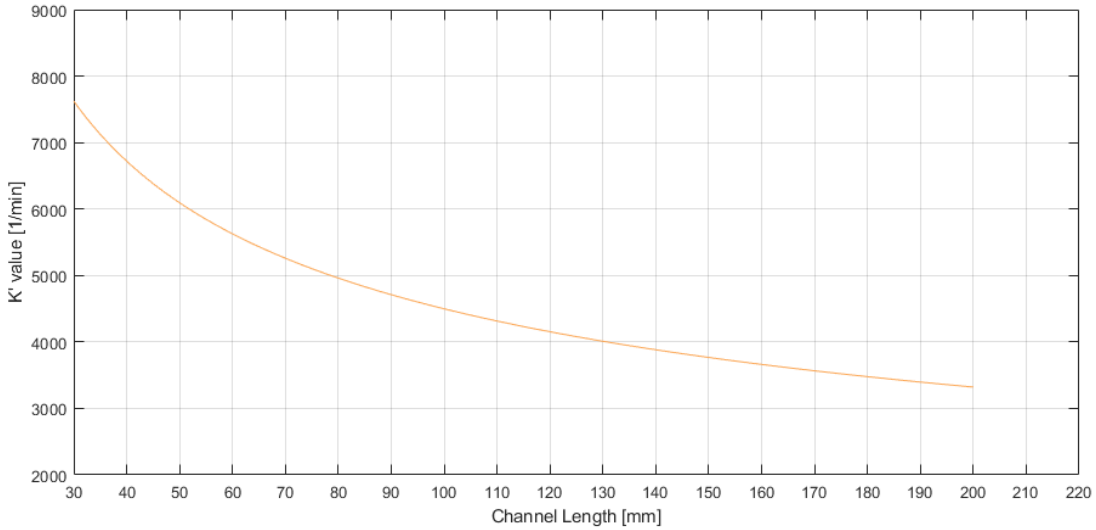

Figure 3.15: K' as function of channel length.

The model can predict the final wavelength, the K' and C_{Cl} that samples will have according to the flux limiter design parameters (channel length, channel diameter, number of channels and substrate dimension) but also according to the process parameters (deposition pressure, temperature and parylene thickness, which is strictly related to time). The K' trend in function of channel length is reported in Figure 3.15.

The ion exchange reaction kinetics have been found considering the wavelength obtained according to reaction time (see Appendix B for the fitting trend). It was found that the reaction order is equal to 4.4608.

$$R_{exchange} = K_{exchange} C^n \quad \textbf{3.8}$$

During the extension of the process to a bigger substrate, used in LED device fabrication, it was noticed that the substrate dimension influence the required amount of chlorine. This means that different substrate dimensions will require different optimal design parameters for the flux limiter. The model is also able to account for these changes.

The K' follows a power law (ax^b) with respect to the length of the channel. This behavior is in accordance with the mass transfer through a cylindrical channel that is given by:

$$\frac{K_d}{D} = 1.62 \left(\frac{d^2 v_0}{LD} \right)^{1/3} \quad \textbf{3.9}$$

Where K_d is the mass transfer coefficient, D is the diffusion coefficient, d is channel diameter, L is the length and v_0 is the average velocity in the tube.

Mass transfer coefficient appears to be proportional to $L^{-1/3}$. In the model the value of K' is proportional to L^n, where n is equal to -0.4379, which indicates a similar behavior, considering the approximations applied for the model and numerical solution.

3.3.1. Numerical Solutions

The model is able to predict the correct wavelength with an error of less than 1% for channel length higher than 30 mm. The only limitation that the model has is working under 30mm channel length. To keep the model valid the fitting of K' has to be changed according to experimental data, the trend changes from a potential to an asymptotic trend until it intercepts the K' axis (for channel length equal to zero). It is able to predict all the scenarios, according to flux limiter design parameters.

The reactive species concentration can be evaluated numerically along the channel for every channel length.

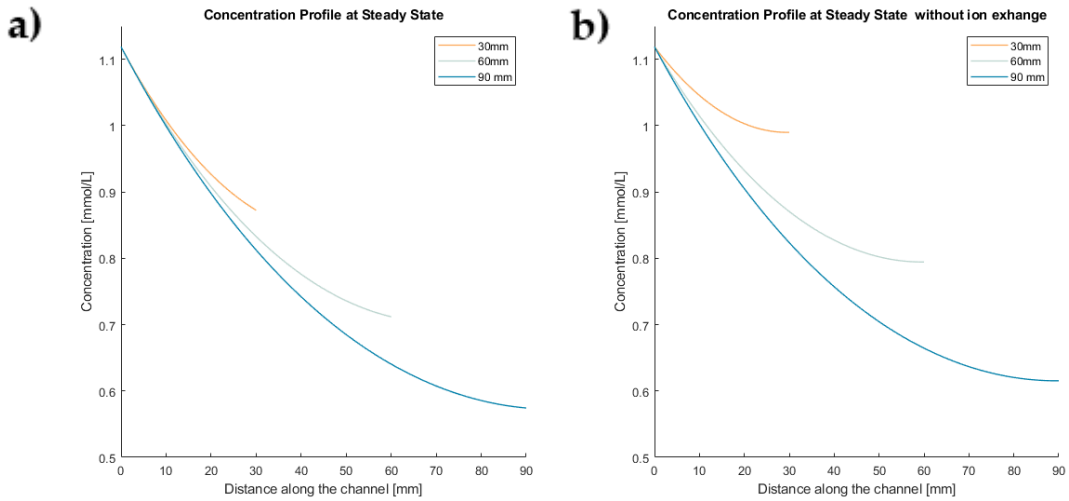

Figure 3.16: Reactant concentration profile at steady state with different FL channel lengths. The figure a) is the profile evaluated accounting for the ion exchange reaction with $CsPbBr_3$, while the figure b) is the profile without considering the reaction. In the figure are represented three different length:30, 60, 90 mm.

As can be seen from Figure 3.16, at the steady state the profile present a curvature and not a linear trend. This is quite normal since that inside the channel the deposition reaction is happening. A linear profile will be obtained only if the reaction inside the channel would have been neglected. The profile without the reaction is less steep due to the absence of a reaction term that consume the monomer at the end of the channel.

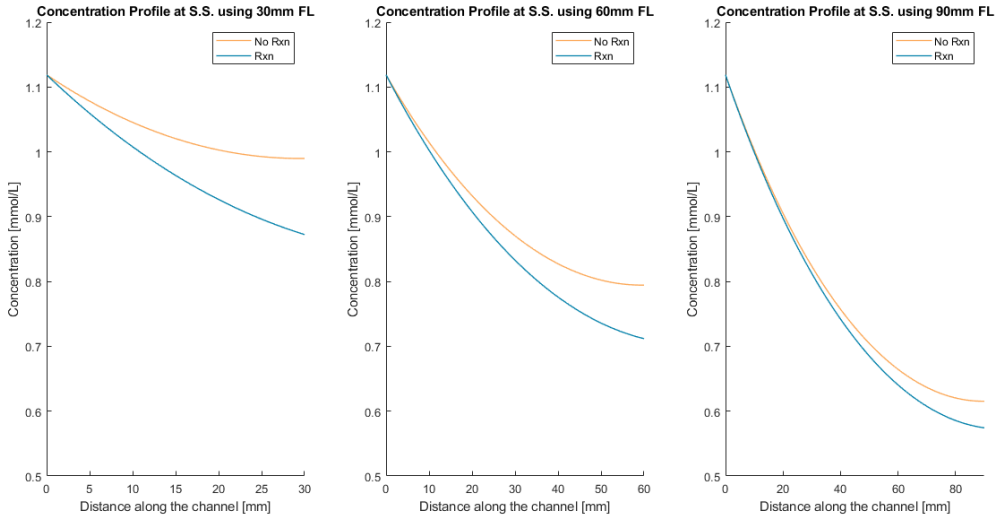

Figure 3.17: Concentration profile at steady state (S.S.) in three different channel length scenarios. The other model parameter as channel diameter, number of channels and substrate dimensions are kept constant and equal to 2mm, 4 and 1 cm^2.

The profiles shown in Figure 3.16 and Figure 3.17 are related only to one channel. The model has been created in way that the sample experiences a concentration that is a multiple of that. It is exactly n times the concentration of a single channel, where n is

the number of channel in the FL. This assumption can be utilized due to the very fast reaction kinetics of exchange (see Appendix B). In Figure 3.16 and Figure 3.17 it can be noticed that increasing channel lengths, the diffusion and the deposition are more restrictive and it permits less material to reach the sample.

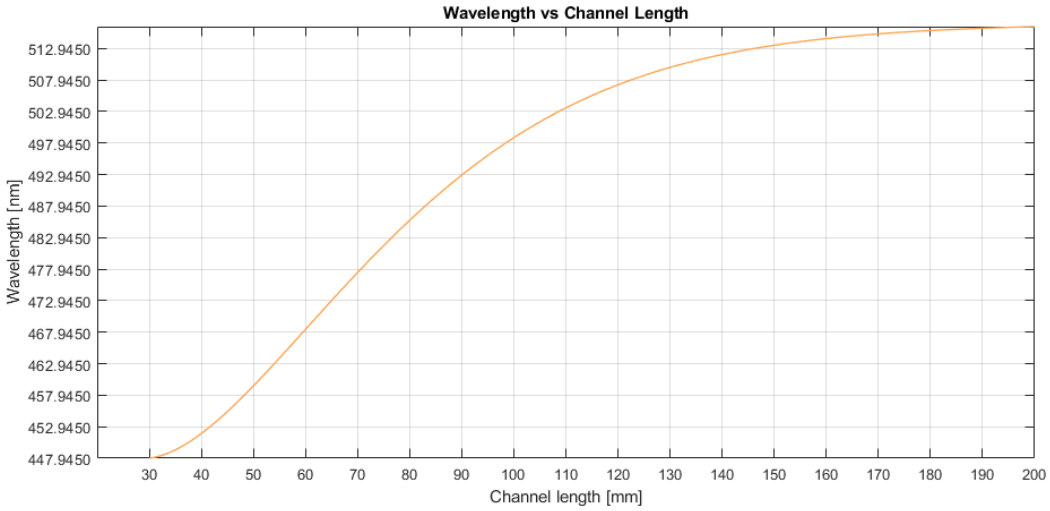

Figure 3.18: Wavelength in function of the channel length

Figure 3.18 illustrates how the emission wavelength due to ion exchange changes with channel length changes. Increasing the length until 90 mm the trend seems to be linear. After that it flattens out until it reaches a plateau. That feature is explained because increasing the length too much causes the concentration to decrease significantly due to stronger diffusion limitation. The diffusion contribution to mass transport and the wall deposition reaction become comparable. The diffusion effect is counter balanced by the deposition of monomer and the active species won't reach the sample, reducing the reaction conversion until it reaches zero.

Cs HI	Channel Length [mm]		
	30	45	60
Experimental results	447.73 [nm]	453 [nm]	462.03 [nm]
Numerical results	443.47 [nm]	450.77 [nm]	464.28 [nm]

Table 6: Emission wavelength resulted from experiments and numerical evaluation Cs HI NCs. The FL design parameter were: 4 channel length, 3mm diameter and 1 cm^2 substrate. The deposited parylene was kept at 50 nm for all the measurements.

MA/FA	Channel Length [mm]				
	30	45	60	65	70
Experimental results	445.47 [nm]	455.26 [nm]	467.047 [nm]	471.25 [nm]	474.07 [nm]
Numerical results	446.47 [nm]	454.22 [nm]	467.38 [nm]	472.01 [nm]	476.55 [nm]

Table 7: Wavelength resulted from experiments and numerical evaluation for MA/FA NCs. The FL model parameter were: 4 channel length, 2mm diameter and 1 cm^2 substrate. . The deposited parylene was kept at 50 nm for all the measures.

As can be observed in Table 6 and Table 7 the difference in experimental and numerical evaluation is quite small. So the model can be used to predict, with high accuracy, the wavelength that a sample will have after exchange process. A similar simulation has been evaluated for different thicknesses of the deposited film. Since the process proceeds at constant pressure, the concentration in the environment will always remain the same when changing the amount of parylene to be deposited. In that way the only variable to be changed inside the model is the time, because it will be the responsible for different film thicknesses since the flux inside the chamber will always stay the same for a given channel length.

MA/FA	Film of Parylene deposited [nm]				
	25	50	100	200	500
Experimental reference	496.36 [nm]	467.047 [nm]	461.03 [nm]	452.25 [nm]	449.233 [nm]
Numerical Reference	490.47 [nm]	467.37 [nm]	460.87 [nm]	442.10 [nm]	426.94 [nm]

Table 8:Numerical and experimental results changing Film of Parylene deposited.

In Table 8 the numerical results of different film thickness are evaluated by changing the deposition time according to the previously stated reasoning. As can be seen, higher thickness numerical evaluation does not match anymore the experimental results. This deviation results from the fact that the model uses experimental data of a 50 nm deposition to fit the reaction kinetics and could therefore not applicable for other thicknesses. Another reason for the deviation could arise the effect that thicker deposited film will prevent further Cl atoms to reach the sample surface. In that way

a diffusion resistance opposes again the ion exchange reaction limiting it. This should be a reason why it reaches a plateau after a certain amount of parylene is deposited.

3.4. Investigation on Ion Exchange

To confirm that the colour shift was effectively carried out by an ion exchange reaction several characterization methods were performed. The aim was also to understand the behavior of the reaction.

The characterization process requires to determine how much Parylene is effectively deposited on the sample inside the FL. This is important because Parylene-C is a dielectric and thicknesses above 10 nm will be detrimental to electron transport if used for actively emitting materials in LED applications.

Different techniques and instruments have been used to study the system, among which: XRD, UV-Vis spectroscopy, SEM, reactive ion etching and profilometry .

3.4.1. Profilometry

Profilometer has been used primarily to determine the thickness of the parylene film deposited on a silicon substrate. The results were in accordance with the one shown in Table 1, with small error around 20nm for higher thicknesses. Instead for 50, 100 and 200 nm the resulted thickness was close to the expected values. This is extremely important in order to keep a good process reproducibility. The measurements have been performed by etching part of the polymer present on the substrate in order to obtain a perfect step. Half of substrate covered with parylene film has been etched with a reactive oxygen plasma using a mask as protection for the non-etched side (Figure 3.19). The parameter for etching has been chosen in according to a previous study according to the expected thickness of the parylene film [102].

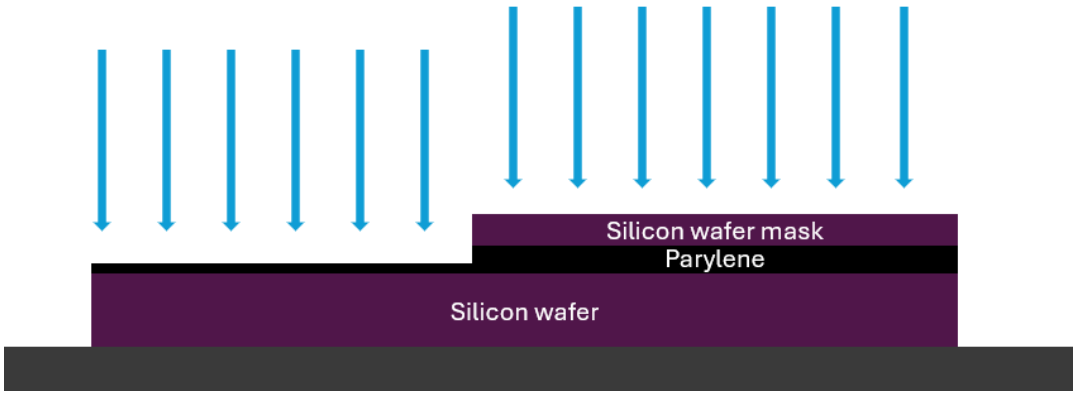

Figure 3.19: Parylene etching using silicon wafer as protection mask.

The same measurements have been done also for silicon substrate placed inside flux limiter. A deposition run with 4 grams of DPX-C has been done for a substrate inside FL and outside it. Has been found that the amount of parylene deposited in the sample

inside is more than ten times less than the amount deposited outside the FL. The sample within the FL showed a film thickness around 160 nm (with FL 60mm, 4 channels and 2 mm diameter), compared to the regular 2 micrometer thickness that is usually obtained by a regular deposition process.

3.4.2. UV-Vis spectroscopy

UV-Vis spectroscopy has been used to ensure that the absorbance features of the NCs are not significantly altered and show similar optical behaviour compared to other anion exchange methods. As reported in Figure 1.5 and in Figure 1.5 the behaviour of a quantum-confined system shows different features from weakly confined structures. The absorbance curve shows an excitonic peak in a confined system. Instead for the other system, where the quantum confinement is not reached, the behaviour is approximately monotonously increasing with decreasing wavelength.

The UV-Vis has been used to give a first confirmation of a purely chemical alteration of the reacted NCs.

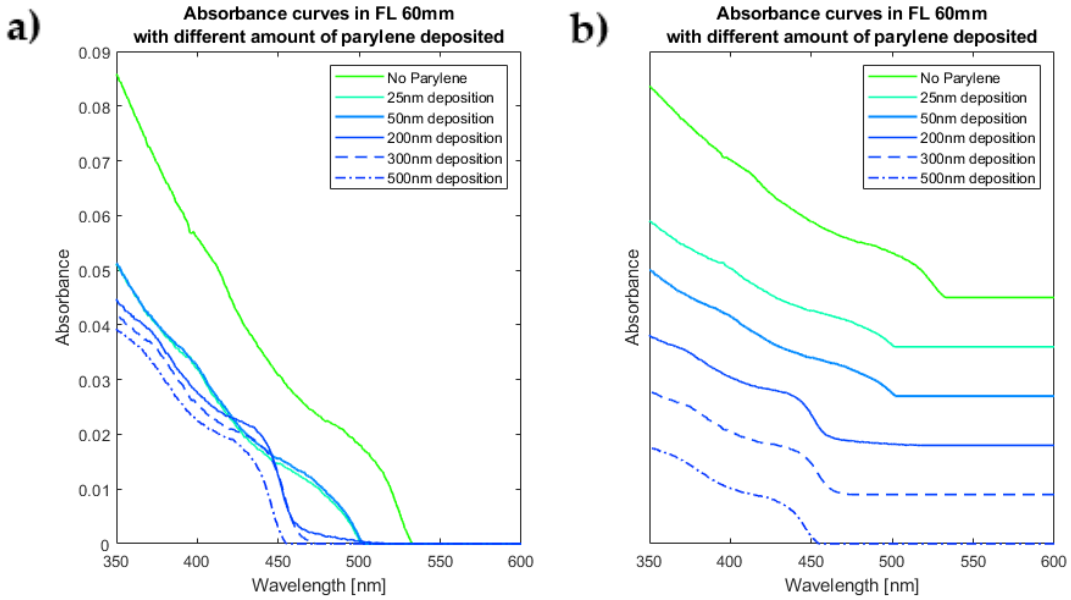

Figure 3.20: Absorbance vs wavelength. a)normal overlap absorbance spectrum; b) offset absorbance spectrum.

Figure 3.20 compares the absorbance behavior of LHP-NCs under different conditions. The plots indicate maximum absorbance decreases with a blue shift in the emission spectrum, quite contrary to quantum-confined systems. In quantum confinement, sharp and pronounced excitonic peaks are a characteristic signature of nanocrystals due to the confinement of the charge carriers in the small volume. Most importantly absorbance edge of the LHP-NCs is increasingly blueshifted with increasing parylene thickness. This is expected as more chlorine is incorporated into the NCs, shifting the band gap to higher energies. In addition, an increase in the parylene layer thickness is

accompanied by a decrease in absorbance, which suggests degradation dependent on both the ion-exchange reaction and vacuum conditions within the coating apparatus.

3.4.3. XRD

XRD has been used to evaluate changes in distance between crystal planes. It is related to the theta through the relation reported in Equation 2.3.

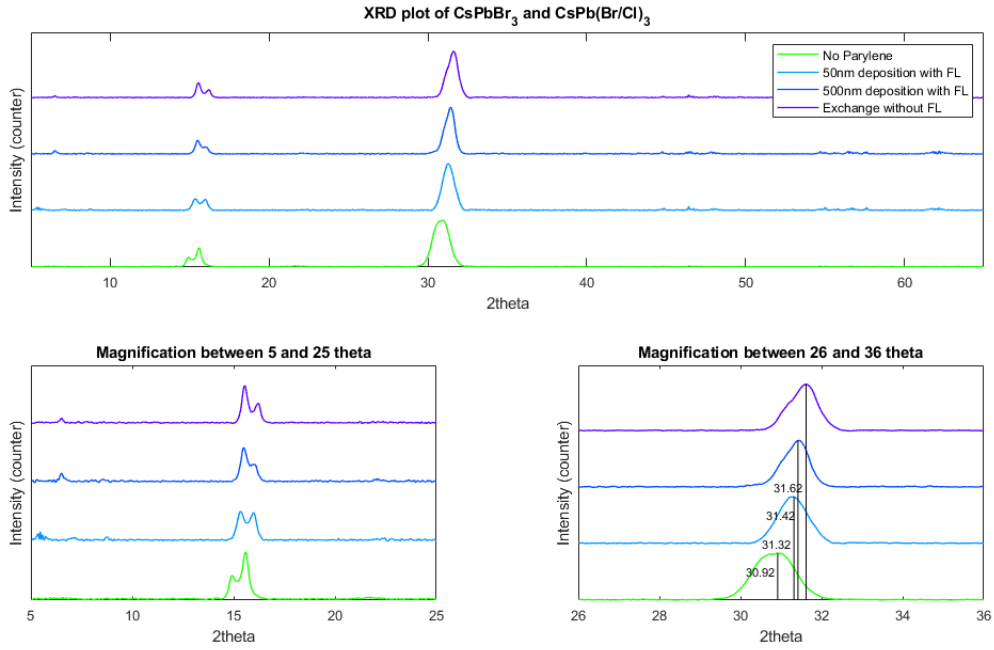

Figure 3.21: XRD measurement of 50nm and 500nm using FL, sample without parylene and shifted sample without diffusion limitation approach.

Figure 3.21 represents the XRD patterns with background removal. The measurements have been performed using silicon wafers as substrates. The film is deposited by spin coating using the same parameters as the ones used for parylene coater samples. An additional denoising process has been done to remove the silicon substrate peaks, in order to highlight the perovskites peaks (see appendix C). The graphs present different shape and position of relevant peaks. As can be seen in Figure 3.21 they change in shape and position. This change is small if we have a look to incident angle. It means that the distance between the planes 100 (between 10 and 20 theta) and 200 (around 30 theta) is changed by a small degree after the exchange reaction. The small contraction is due to the different halogen dimension. Since Cl is smaller than Br the exchange causes the NCs to contract in order to decrease the free energy and reach a new equilibrium state .

3.4.4. SEM

A scanning electron microscope (Zeiss ULTRA 55 plus) has been used in order to identify a possible difference in NCs structure after ion exchange. Parylene, if present

at higher thicknesses, represents a barrier to the electrons that are send to the sample. Since the strong isolating nature of the polymer it has not been possible to look at thicker films but only to small film as 50 nm. A sample treated with parylene inside the FL is expected to only have a few nm of a homogenous film or the presence of multiple polymerization clusters. Since the concentration of monomer that reach the sample is quite low, looking at experimental results reported in Table 1, the parylene film will be homogenous at least in the case of 50, 100, 200, 500 nm deposition. So in that way it should be possible to recognise the non-conductive polymer from the NCs sample inside FL. The NCs used are the Cs HI because thanks to the inorganic centre they are easier to detect and visualize.

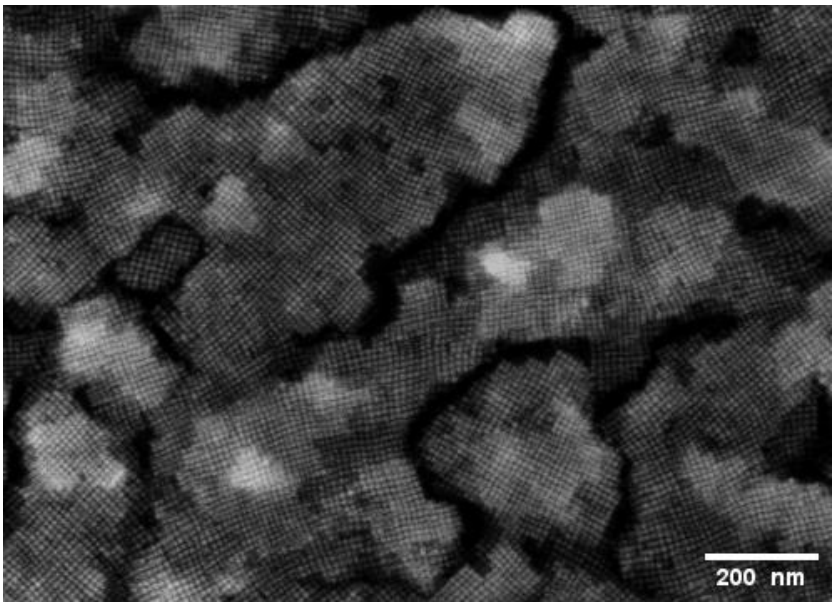

Figure 3.23: SEM image of $CsPbBr_3$ NCs by HI method

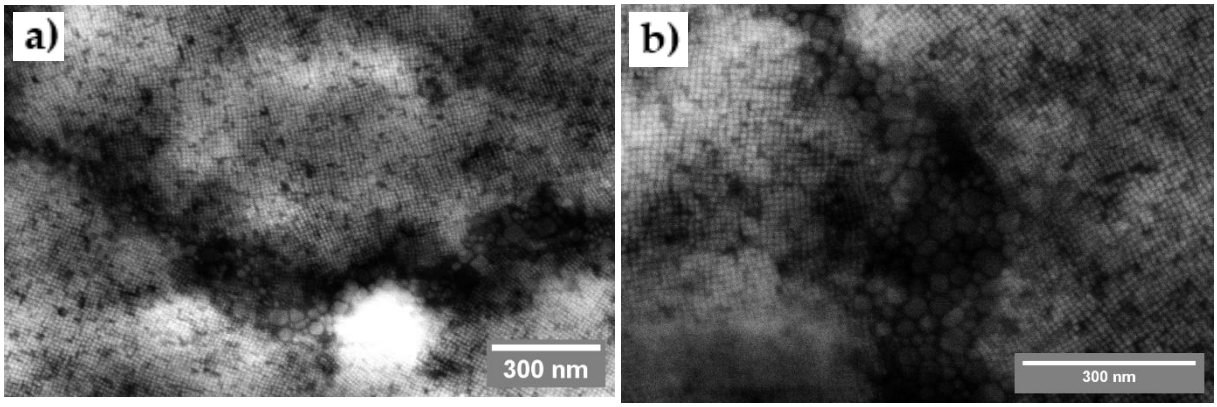

Figure 3.22: SEM images of 50nm deposited film on a $CsPbBr_3$ sample. photo on the right is a zoom of the left photo inside a crack.

As can be seen from Figure 3.23 the film presents more or less the same orientation and pattern with respect to Figure 3.22. The only difference is related to the presence of circular structures. These structures are visible in Figure 3.22 a) but even more in Figure 3.22 b), that is a magnification of the previous inside one crave. They are quite

bigger than NCs and appear different, similar to bubbles. Only the shape can be detected well and inside seems to show a distorting noise, typical for not conductive materials. These structures are likely to be nucleation clusters. The reason for that might be because of the homogeneity of the film, inside the cracks the perovskites film appear to be less homogenous and a nucleation is favoured because the area per unit square will be higher if compared with a perfectly planar surface. The parylene film ,if compared with a deposition done on a substrate without NCs film, is heterogenous. There are more reasons for that behaviour: the deposition area is not anymore perfectly as the silicon wafer area, the surface is not anymore activated by oxygen plasma and some solvent that is still present one the sample can evaporates following preferential path that reduce the film homogeneity. 50 nm of parylene, if present in a homogenous film would be able to block the signal obscuring completely the image without being able to observe any NCs.

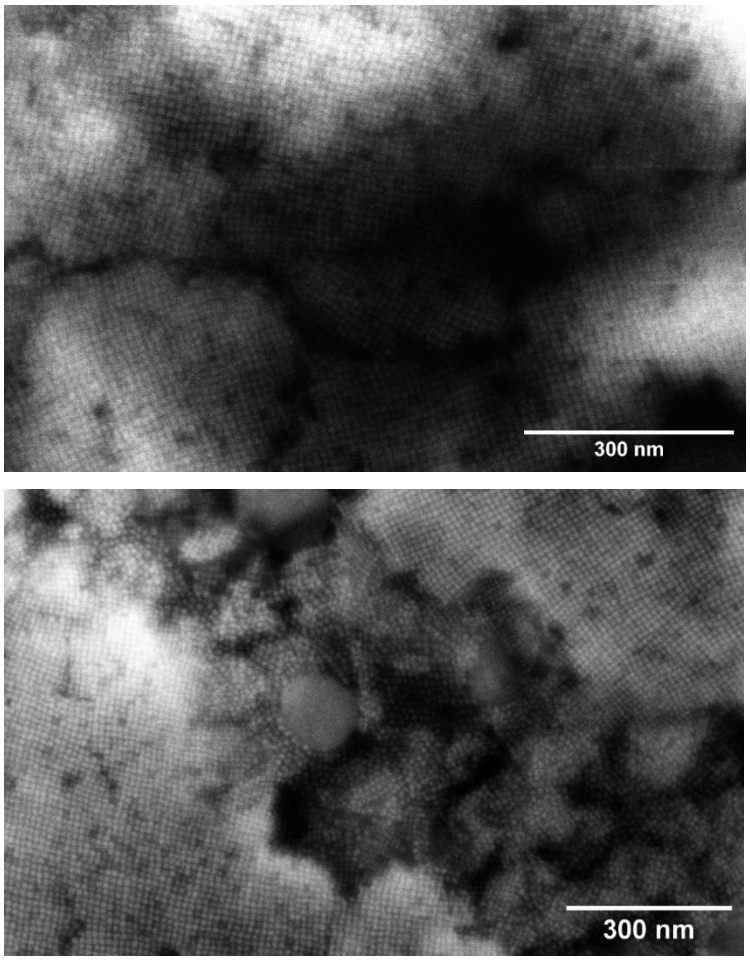

Figure 3.24: SEM photo of 50 nm deposition using Flux Limiter with 4 channel, 60 mm channel length and 2 mm diameter.

Samples exchanged inside the flux limiter have been shown to produce a lesser blueshift thanks to diffusion limitation and therefore a lesser amount of parylene deposited on them. In Figure 3.24 parylene clusters are less and with smaller

dimensions compared to the ones in Figure 3.22 b). So the flux limiter effectively limits polymer growing, limiting the conversion of the reaction.

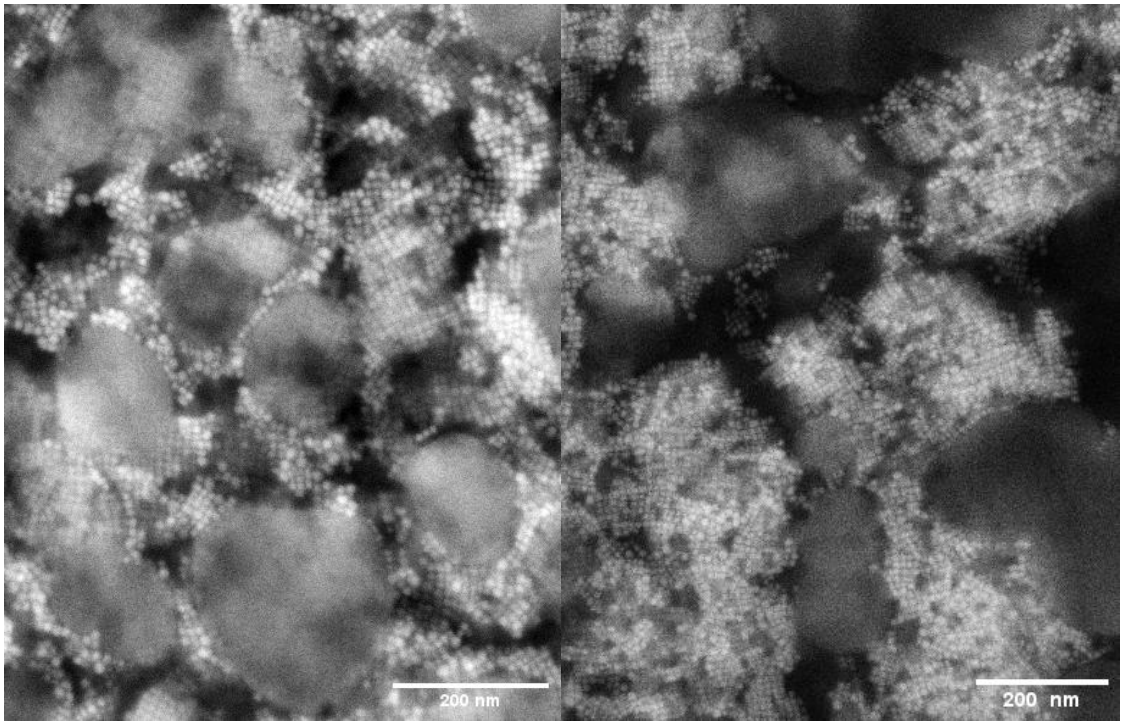

Figure 3.25: SEM photo of 500 nm deposition using Flux Limiter with 4 channel, 60 mm channel length and 2 mm diameter.

Another example is reported in Figure 3.25 where this time the amount of dimer used is one gram, which corresponds to 500 nm of deposited film. Cluster dimensions if compared with Figure 3.24 are bigger, due to the larger amount of time and amount of polymer deposited during the process. As can be seen thanks to the high resolution it is possible to see through the clusters even if with poor resolution. Under the bubbles NCs are observable.

3.4.5. First observation of reaction mechanism

The reaction mechanism seems to be strictly connected to the ligands.

It is used perovskites sample, previously analysed with SEM, in this study. This sample was spin coated with Cs HI (the same used for exchange, without changes). The exchange happened but only in regions where the electron beam was not used. The electron beam has enough energy to burn the ligands, converting them in carbon. Since the exchange did not happen (or happen but with less conversion) in that regions where the NCs were free of ligands, a possible explanation can be because the ligands works as medium for the reaction.

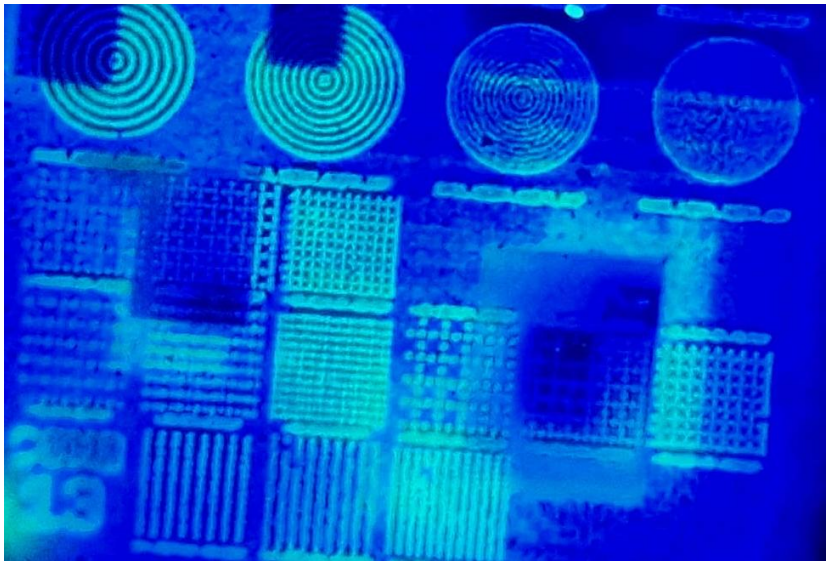

Figure 3.26: Silicon substrate with patterns made with Cs HI. The sample has first been imaged by and then coated with parylene to observe a shift in color.

In that way it is used bulks perovskites (free of ligands), made with evaporation deposition, to prove again this phenomena. The exchange and the wavelength shift had not be observed using this king of perovskites.

4 Conclusion and Outlook

The work has illustrated an effective and precise emission wavelength tuning in lead halide perovskites by the parylene-C-assisted gas-solid phase reaction. The present work uncovers the process of ion exchange, which involves diffusion limitations and the solutions to such limitations in order to boost stability and efficiency for blue-emitting LHP NCs.

The key findings include formulating the numerical model, which is able to predict the result of the ion exchange process, and a significant advancement in understanding on the ability to control of the emission properties. It has been demonstrated that controlled modulation of green-to-blue emission characteristics of LHP-NCs can be realized by careful management of the gas-phase ion-exchange process during parylene deposition, thus opening new possibilities for their application in high-performance and cost-effective optoelectronic devices.

LHP-NCs are regarded as very promising candidates with high potential in the field of LEDs, laser and photodetectors due to their precisely tunable and pure emission features. This work permits setting up devices with tailored spectra of emissions, high efficiencies, and possibly significantly reduced expenses connected with their production due to the scalable nature of the gas-solid phase reaction process.

For now, several exciting directions can be further expanded from these findings in the future. In this regard, one approach could be a change of parylene type to include bromine and starting LHPs containing iodine; such an approach will result in tonalities of red shift, increasing colour tuning opportunities and thus boosting the versatility of this reaction platform for LHP-NCs within a wide range of applications.

Moreover, additional improvement in the numerical prediction model and construction of a detailed mechanism for the reaction will provide deeper insight into the ion-exchange process. Provided a comprehensive understanding of the mechanism, this also allows for even finer control of the emission properties, which further enables better design strategies toward LHP-based devices.

A detailed study on the effect of vacuum pressure could reveal valuable information about the stability and performance of LHPs under different environmental conditions. The findings could improve the understanding of the practical use of LHP-NCs under real application conditions that vary in pressures, such as deposition steps during LED manufacturing.

Finally, the possibility of integrating these optimized blue-emitting LHP-NCs into different optoelectronic devices, their performance evaluation, and other possible practical application can be considered for future investigation. That means that the

investigation of their long-term stability and durability under operational conditions will also turn out to be quite critical in terms of commercializing these materials.

In summary, this thesis has provided a solid base for the accurate control of the emission wavelengths of LHPs through a new gas-solid phase ion-exchange reaction. The results have offered not only insights into the nature of these materials but also potential applications in state-of-the-art optoelectronic technology. Further efforts on this subject are surely foreseeable for the creation of next-generation devices with more desirable performance and efficiency.

Bibliography

[1] L. Protesescu *et al.*, "Nanocrystals of Cesium Lead Halide Perovskites ($CsPbX_3$, X = Cl, Br, and I): Novel Optoelectronic Materials Showing Bright Emission with Wide Color Gamut," *Nano Lett*, vol. 15, no. 6, pp. 3692–3696, Jun. 2015, doi: 10.1021/nl5048779.

[2] G. Nedelcu, L. Protesescu, S. Yakunin, M. I. Bodnarchuk, M. J. Grotevent, and M. V. Kovalenko, "Fast Anion-Exchange in Highly Luminescent Nanocrystals of Cesium Lead Halide Perovskites ($CsPbX_3$, X = Cl, Br, I)," *Nano Lett*, vol. 15, no. 8, pp. 5635–5640, Aug. 2015, doi: 10.1021/acs.nanolett.5b02404.

[3] Y. Shirasaki, G. J. Supran, M. G. Bawendi, and V. Bulović, "Emergence of colloidal quantum-dot light-emitting technologies," *Nat Photonics*, vol. 7, no. 1, pp. 13–23, Jan. 2013, doi: 10.1038/nphoton.2012.328.

[4] L. Qian, Y. Zheng, J. Xue, and P. H. Holloway, "Stable and efficient quantum-dot light-emitting diodes based on solution-processed multilayer structures," *Nat Photonics*, vol. 5, no. 9, pp. 543–548, Sep. 2011, doi: 10.1038/nphoton.2011.171.

[5] S. Coe, W.-K. Woo, M. Bawendi, and V. Bulović, "Electroluminescence from single monolayers of nanocrystals in molecular organic devices," *Nature*, vol. 420, no. 6917, pp. 800–803, Dec. 2002, doi: 10.1038/nature01217.

[6] Y.-H. Won *et al.*, "Highly efficient and stable InP/ZnSe/ZnS quantum dot light-emitting diodes," *Nature*, vol. 575, no. 7784, pp. 634–638, Nov. 2019, doi: 10.1038/s41586-019-1771-5.

[7] G. Konstantatos and E. H. Sargent, "Solution-Processed Quantum Dot Photodetectors," *Proceedings of the IEEE*, vol. 97, no. 10, pp. 1666–1683, Oct. 2009, doi: 10.1109/JPROC.2009.2025612.

[8] P. ; Ramasamy *et al.*, "All-Inorganic Cesium Lead Halide Perovskite Nanocrystals for Photodetector Applications," 2016.

[9] H. ; F. Y. ; M. F. ; W. X. ; G. Z. ; D. Q. ; G. M. V. ; T. M. T. ; J. S. ; Z. X. Y. Zhu, "Lead Halide Perovskite Nanowire Lasers with Low Lasing Thresholds and High Quality Factors," *Natural Material*, vol. 14, pp. 636–642, 2015.

[10] Y.-H. ; P. P. ; A. T. D. Lin, "MetalHalide Perovskite Transistors for Printed Electronics: Challenges and Opportunities," *Advance materials*, vol. 29, p. 1702838, 2017.

[11] M. V. Kovalenko, L. Protesescu, and M. I. Bodnarchuk, "Properties and potential optoelectronic applications of lead halide perovskite nanocrystals," *Science (1979)*, vol. 358, no. 6364, pp. 745–750, Nov. 2017, doi: 10.1126/science.aam7093.

[12] L. N. Quan, B. P. Rand, R. H. Friend, S. G. Mhaisalkar, T.-W. Lee, and E. H. Sargent, "Perovskites for Next-Generation Optical Sources," *Chem Rev*, vol. 119, no. 12, pp. 7444–7477, Jun. 2019, doi: 10.1021/acs.chemrev.9b00107.

[13] X. Jin *et al.*, "Cation exchange assisted synthesis of ZnCdSe/ZnSe quantum dots with narrow emission line widths and near-unity photoluminescence quantum yields," *Chemical Communications*, vol. 56, no. 45, pp. 6130–6133, 2020, doi: 10.1039/D0CC01302A.

[14] H. L. U. Wells, "ber die Casium- und Kalium-Bleihalogenide," *Zeitschrift fuër anorganische Chemie*, vol. 3, pp. 195–210, 1893.

[15] D. Weber, "Das Perowskitsystem CH3NH3[PbSn1 nX3] (X = Cl, Br, I) / The Perovskite System CH3NH3[PbnSn1 nX3] (X = C1, Br, I)," *Z. Naturforsch., B: J. Chem. Sci.* , vol. 34, pp. 939–941, 1979.

[16] D. Weber, "CH3NH3PbX3, ein Pb(II)-System mit kubischer Perowskitstruktur / CH3NH3PbX3, a Pb(II)-System with Cubic Perovskite Structure," *Z. Naturforsch., B: J. Chem. Sci.*, vol. 33, pp. 1443–1445, 1978.

[17] D. Weber, "CH3NH3SnBrxI3 x (x = 0-3), ein Sn(II)-System mit kubischer Perowskitstruktur / CH3NH3SnBrxI3 x(x = 0-3), a Sn(II)- System with Cubic Perovskite Structure," *Z. Naturforsch., B: J. Chem. Sci.*, vol. 33, pp. 862–865, 1978.

[18] D. B. ; C. K. ; K. C. R. Mitzi, "Organic-Inorganic Electronics," 2001.

[19] D. B. ; F. C. A. ; H. W. T. A. ; G. A. M. Mitzi, "Conducting Tin Halides with a Layered Organic-Based Perovskite Structure," *Nature*, vol. 369, pp. 467–469, 1994.

[20] W. ; G. E. N. K. ; B. H. ; S. D. O. ; P. R. G. Travis, "Application of the Tolerance Factor to Inorganic And Hybrid Halide Perovskites: A Revised System," *Chem. Sci.*, vol. 7, pp. 4548–4556, 2016.

[21] J. S. Manser, J. A. Christians, and P. V. Kamat, "Intriguing Optoelectronic Properties of Metal Halide Perovskites," *Chem Rev*, vol. 116, no. 21, pp. 12956–13008, Nov. 2016, doi: 10.1021/acs.chemrev.6b00136.

[22] D. W. ; V. S. M. ; S. S. D. ; N. H. ; E. G. E. ; Z. M. E. ; S. H. J. ; G. D. S. de Quilettes, "Impact of Microstructure on Local Carrier Lifetime in Perovskite Solar Cells," *Science (1979)*, vol. 348, pp. 683–686, 2015.

[23] F. ; B. S. ; T. W. ; H. A. ; G. F. Wang, "Defects Engineering for High-Performance Perovskite Solar Cells," *Flex. Electron*, vol. 2, pp. 22–22, 2018.

[24] H. ; Y. K. Uratani, "Charge Carrier Trapping at Surface Defects of Perovskite Solar Cell Absorbers: A First-Principles Study," *J. Phys. Chem. Lett.* , vol. 8, pp. 742–746, 2017.

[25] M. I. Bodnarchuk *et al.*, "Rationalizing and Controlling the Surface Structure and Electronic Passivation of Cesium Lead Halide Nanocrystals," *ACS Energy Lett*, vol. 4, no. 1, pp. 63–74, Jan. 2019, doi: 10.1021/acsenergylett.8b01669.

[26] Y. Dong *et al.*, "Recent advances toward practical use of halide perovskite nanocrystals," *J Mater Chem A Mater*, vol. 6, no. 44, pp. 21729–21746, 2018, doi: 10.1039/C8TA06376A.

[27] J. Shamsi, A. S. Urban, M. Imran, L. De Trizio, and L. Manna, "Metal Halide Perovskite Nanocrystals: Synthesis, Post-Synthesis Modifications, and Their Optical Properties," *Chem Rev*, vol. 119, no. 5, pp. 3296–3348, Mar. 2019, doi: 10.1021/acs.chemrev.8b00644.

[28] Y. ; B. E. ; A. M. F. ; M. A. ; M. K. Z. ; H. V. A. ; D. P. ; B. S. ; U. A. S. ; P. L. ; F. J. Tong, "Highly Luminescent Cesium Lead Halide Perovskite Nanocrystals with Tunable Composition and Thickness by Ultrasonication," *Angew. Chem.*, vol. 55, 2016.

[29] D. D. ; Y. Y. M. ; B. Y. ; Y. Y. ; G. N. A. ; W. A. B. ; E. S. W. ; K. N. ; K. Q. ; L. M. L. ; A. A. P. ; L. S. R. ; Y. P. D. Zhang, " Synthesis of Composition Tunable and Highly Luminescent Cesium Lead Halide Nanowires through Anion-Exchange Reactions.," *J. Am. Chem. Soc.*, vol. 138, pp. 7236–7239, 2016.

[30] Q. A. Akkerman, "Tuning the Optical Properties of Cesium Lead Halide Perovskite Nanocrystals by Anion Exchange Reactions," *J Am Chem Soc*.

[31] J. A. ; T. Y. ; M. N. ; V. M. ; F. S. ; M. K. Z. ; G. C. R. ; N. B. ; C.-D. C. ; S. J. K. ; U. A. S. ; F. J. Sichert, "Quantum Size Effect in Organometal Halide Perovskite Nanoplatelets," *Nano Lett*, vol. 15, pp. 6521–6527, 2015.

[32] P. ; A. S. M. ; T. W. A. Tyagi, "Colloidal Organohalide Perovskite Nanoplatelets Exhibiting Quantum Confinement," *J. Phys. Chem. Lett.*, vol. 6, pp. 1911–1916, 2015.

[33] Y. ; B. B. J. ; B. E. ; W. K. ; M.-B. P. ; B. S. ; U. A. S. ; P. L. ; F. J. Tong, "From Precursor Powders to CsPbX3 Perovskite Nanowires: One-Pot Synthesis, Growth Mechanism, and Oriented Self-Assembly.," *Angew. Chem*, vol. 56, pp. 13887–13892, 2017.

[34] C. B. ; N. D. J. ; B. M. G. Murray, "Synthesis and Characterization of Nearly Monodisperse CdE (E = Sulfur, Selenium, Tellurium) Semiconductor Nanocrystallites," *J. Am. Chem.*, vol. 115, pp. 8706–8715, 1993.

[35] B. ; R. M. V. ; F. R. A. Zorman, "Quantum Confinement Effects in CdSe Quantum Dots," *J. Phys. Chem*, vol. 99, pp. 7649–7653, 1995.

[36] A. P. Alivisatos, A. L. Harris, N. J. Levinos, M. L. Steigerwald, and L. E. Brus, "Electronic states of semiconductor clusters: Homogeneous and inhomogeneous broadening of the optical spectrum," *J Chem Phys*, vol. 89, no. 7, pp. 4001–4011, Oct. 1988, doi: 10.1063/1.454833.

[37] C. B. Murray, C. R. Kagan, and M. G. Bawendi, "Synthesis and Characterization of Monodisperse Nanocrystals and Close-Packed Nanocrystal Assemblies," *Annual Review of Materials Science*, vol. 30, no. 1, pp. 545–610, Aug. 2000, doi: 10.1146/annurev.matsci.30.1.545.

[38] M. A. Kastner, "Artificial Atoms," *Phys Today*, vol. 46, no. 1, pp. 24–31, Jan. 1993, doi: 10.1063/1.881393.

[39] R. C. Ashoori, "Electrons in artificial atoms," *Nature*, vol. 379, no. 6564, pp. 413–419, Feb. 1996, doi: 10.1038/379413a0.

[40] A. L. Efros and A. L. Efros, "Interband absorption of light in a semiconductor sphere," *Sov. Phys. Semicond.*, vol. 16, pp. 772–775, 1982.

[41] L. Brus, "Electronic wave functions in semiconductor clusters: experiment and theory," *J Phys Chem*, vol. 90, no. 12, pp. 2555–2560, Jun. 1986, doi: 10.1021/j100403a003.

[42] D. A. Hanifi *et al.*, "Redefining near-unity luminescence in quantum dots with photothermal threshold quantum yield," *Science (1979)*, vol. 363, no. 6432, pp. 1199–1202, Mar. 2019, doi: 10.1126/science.aat3803.

[43] P. Reiss, J. Bleuse, and A. Pron, "Highly Luminescent CdSe/ZnSe Core/Shell Nanocrystals of Low Size Dispersion," *Nano Lett*, vol. 2, no. 7, pp. 781–784, Jul. 2002, doi: 10.1021/nl025596y.

[44] L. Qu and X. Peng, "Control of Photoluminescence Properties of CdSe Nanocrystals in Growth," *J Am Chem Soc*, vol. 124, no. 9, pp. 2049–2055, Mar. 2002, doi: 10.1021/ja017002j.

[45] "'BT Series, 2100: Image parameter values for high dynamic range television for use in production and international programme exchange; https://www.itu.int/rec/R-REC-BT.2100-2-201807-I/en'.".

[46] H. J. Queisser and E. E. Haller, "Defects in Semiconductors: Some Fatal, Some Vital," *Science (1979)*, vol. 281, no. 5379, pp. 945–950, Aug. 1998, doi: 10.1126/science.281.5379.945.

[47] F. P. García de Arquer, D. V. Talapin, V. I. Klimov, Y. Arakawa, M. Bayer, and E. H. Sargent, "Semiconductor quantum dots: Technological progress and future challenges," *Science (1979)*, vol. 373, no. 6555, Aug. 2021, doi: 10.1126/science.aaz8541.

[48] O. E. , L. J. M. , B. M. C. Semonin, "Quantum dots for next-generation photovoltaics," vol. 11, pp. 508–515, 2012.

[49] G. Xing *et al.*, "Long-Range Balanced Electron- and Hole-Transport Lengths in Organic-Inorganic CH 3 NH 3 PbI 3," *Science (1979)*, vol. 342, no. 6156, pp. 344–347, Oct. 2013, doi: 10.1126/science.1243167.

[50] Y. Wang *et al.*, "Reliable Measurement of Perovskite Solar Cells," *Advanced Materials*, vol. 31, no. 47, Nov. 2019, doi: 10.1002/adma.201803231.

[51] Y. Lekina and Z. X. Shen, "Excitonic states and structural stability in two-dimensional hybrid organic-inorganic perovskites," *Journal of Science: Advanced Materials and Devices*, vol. 4, no. 2, pp. 189–200, Jun. 2019, doi: 10.1016/j.jsamd.2019.03.005.

[52] S. D. X. Q. S. K. H. I. N.U. Yasuo Nakayama, "Electronic Processes in Organic Crystals," *Oxford University Press*, vol. 2, 2015.

[53] J. V. I. Pelant, "Luminescence of excitons," *Lumin. Spectrosc. Semicond*, pp. 161–204, 2012.

[54] W. , M. N. , I. O. , N. M. K. , & G. M. Tress, "Predicting the Open-Circuit Voltage of CH3NH3PbI3 Perovskite Solar Cells Using Electroluminescence and Photovoltaic Quantum Efficiency Spectra: The Role of Radiative and Non-Radiative Recombination," *Adv Energy Mater*, 2015.

[55] S. K. , Y. M. , P. N. , K. N. , & H. S. Balakrishnan, "Role of Surface Passivation in Mixed-Halide Perovskite Light-Emitting Diodes," *Advanced Materials*, vol. 28, pp. 7006–7013, 2016.

[56] "Sharma, S.; Weiden, N.; Weiss, A. Z. Phys. Chem. 1992, 175, 63−80.".

[57] J. Pan, "Highly Efficient Perovskite-Quantum-Dot Light-Emitting Diodes: Microscopic Mechanism and Stability.," *Nano Lett*, 2017.

[58] R. K. Behera, "Low-temperature solvothermal synthesis of high-quality $CsPbCl_3$ perovskite nanocrystals.," *J Mater Chem*, 2018.

[59] D. Zhu, "Facile solvothermal synthesis of $CsPbX_3$ (X = Cl, Br, I) perovskite nanocrystals," *Chemistry of Materials*, 2016.

[60] Q. Zhang, "Hydrothermal synthesis of $CsPbX_3$ (X = Cl, Br, I) perovskite nanocrystals with controlled optical properties," *Chemical Communications*, 2016.

[61] Y. Wei, "Microwave-assisted synthesis of cesium lead halide perovskite nanocrystals and their tunable optical properties.," *J Mater Chem*, pp. 804–810, 2016.

[62] F. Zhang, "Fast and facile synthesis of highly luminescent $CsPbX_3$ (X = Cl, Br, I) perovskite nanocrystals via microwave irradiation.," *Materials Letters*, pp. 205–207, 2017.

[63] S. Pathak *et al.*, "Perovskite Crystals for Tunable White Light Emission," *Chemistry of Materials*, vol. 27, no. 23, pp. 8066–8075, Dec. 2015, doi: 10.1021/acs.chemmater.5b03769.

[64] H. , W. L. , T. Y. , and Z. H. Hu, "Room-temperature synthesis of cesium lead halide perovskite nanocrystals by ligand-assisted reprecipitation method," *J Mater Chem*, 2016.

[65] J. ; R. P. ; C. V. ; A. A. L. ; S. D. ; M. L. ; K. R. Shamsi, "Bright-Emitting Perovskite Films by LargeScale Synthesis and Photoinduced Solid-State Transformation of CsPbBr3 Nanoplatelets," *ACS Nano*, vol. 11, 2017.

[66] K.-H. ; W. L. ; L. L. ; Y. H.-B. ; Q. H.-S. ; Y. S.-H. Wang, "Large-Scale Synthesis of Highly Luminescent Perovskite-Related CsPb2Br5 Nanoplatelets and Their Fast Anion Exchange," *Angew. Chem*, vol. 55, 2016.

[67] "Akkerman, Q. A.; D'Innocenzo, V.; Accornero, S.; Scarpellini, A.; Petrozza, A.; Prato, M.; Manna, L. J. Am. Chem. Soc. 2015, 137, 10276.".

[68] "Trots, D. M.; Myagkota, S. V. J. Phys. Chem. Solids 2008, 69, 2520−2526.".

[69] "Stoumpos, C. C.; Malliakas, C. D.; Kanatzidis, M. G. Inorg. Chem. 2013, 52, 9019−9038".

[70] "Babin, V.; Fabeni, P.; Nikl, M.; Nitsch, K.; Pazzi, G. P.; Zazubovich, S. Phys. Status Solidi B 2001, 226, 419−428.".

[71] D. , D. Y. , Q. T. , R. D. , S. D. H. Parobek, "Photoinduced Anion Exchange in Cesium Lead Halide Perovskite Nanocrystals," *J Am Chem Soc*, 2017.

[72] "https://www.physics.rutgers.edu/~podzorov/parylene%20properties.pdf".

[73] A. G. M. B. J. R. and C. C. Krzysztof Smalara, "Theoretical Study of Polymerization Mechanism of p-Xylylene Based Polymers," *J. Phys. Chem*, vol. 114, 2010.

[74] "I.B. Fortin and T.-M. Lu, Chem. Mater. 14, 1945(2002).".

[75] "S. Rogojevic, J .A. Moore, and W.N. Gill, J. Vac. Sci. Techno!. A 17(1), 266(1999).".

[76] J.B.Fortin, "Poly-para-xylylene Thin Films: A Study of the Deposition Chemistry, Kinetics, Film Properties, and Film Stability," *PhD thesis*, 2001.

[77] "W.F. Beach, Macromolecules 11(1), 72(1978).".

[78] "W. Beach, C. Lee, and D. Bassett, Encyclopedia of Polymer Science and Engineering (Wiley, New York, 1985), 17, 990.".

[79] "J.F. Gaynor, Electrochemical Society Proc. V97-8, 176(1997).".

[80] J. B. ; L. T. M. Fortin, *Chemical Vapor deposition polymerization: the growth and properties of parylene thin films*. 2004.

[81] "Szwarc, M. Some Remarks on the CH2dC6H4dCH2 Molecule. Discuss. Faraday Soc. 1947, 2, 46–49.".

[82] W. F. Gorham, " A New General Synthetic Method for Preparation of Linear Poly-P-Xylylenes," *J. Polym. Sci. Polym. Chem.*, vol. 4, pp. 3027–3039, 1966.

[83] "E.M. Charlson, E.J. Charlson, and R. Sabeti, IEEE Transactions on Biomedical Engineering 33(2), 202(1992).".

[84] "F.E. Cm'iou, D.J. Vally, and W.E. Loeb, IEEE Trans. Parts, Mater. Pacakg., 54(1965) ".

[85] "P. Kramer, A.K. Sharma, E.E. Hennecke, and H. Yasuda, Journal of Polymer Science 22,475(1984).".

[86] "S. Ganguli, Ph.D. Thesis, Rensselaer Polytechnic Institute, Troy, NY, 1997.".

[87] "G.-R. Yang, S. Ganguli, J. Karcz, W. Gill, and T.-M. Lu, .1. Crystal Growth 183(3), 385(1998).".

[88] J. D. K. M. Man P F, "Microfluidic plastic capillaries on silicon substrates: A new inexpensive technology for bioanalysis chips.," *IEEE Micro Electro Mechanical Systems*, 1997.

[89] M. C. H. Webster J R, "Large-volume integrated capillary electrophoresis stage fabricated using micromachining of plastics on silicon substrates," *Int. Conf. Solid-State Sensors and Actuators*, 1997.

[90] M. C. H. Carlen E T, "Electrothermally activated paraffin microactuators," 2002.

[91] W. K. D. Rich C A, "An 8-bit microflow controller using pneumatically actuated microvalves," 1999.

[92] "Yang X, Yang J M, Wang X Q, Meng E, Tai Y C, Ho C M 1998 Micromachined membrane particle filters. Proc. IEEE Micro Electro Mechanical Systems (MEMS), Heidelberg, Germany, pp. 137–42".

[93] "Olson R 1989 Parylene conformal coatings and their applications for electronics. Proc. 19th Electrical Electronics Insulation Conference, Electrical Electronics Insulation, Chicago, IL, USA, pp. 272–3".

[94] "Selbrede S C, Zucker M L 1997 Characterization of Parylene-N thin films for low-k VLSI applications. Low-dielectric Constant Materials III, Materials Society Symposium Proceedings, Santa Clara, CA: USA, Vol. 476, pp. 219–24".

[95] J. Zhou *et al.*, "An ultra-thin chemical vapor deposited polymer interlayer to achieve highly improved stability of perovskite solar cell," *Chemical Engineering Journal*, vol. 461, p. 141914, 2023, doi: https://doi.org/10.1016/j.cej.2023.141914.

[96] H.-R. Kim *et al.*, "Cesium Lead Bromide (CsPbBr3) Perovskite Quantum Dot-Based Photosensor for Chemiluminescence Immunoassays," *ACS Appl Mater Interfaces*, vol. 13, no. 25, pp. 29392–29405, 2021, doi: 10.1021/acsami.1c08128.

[97] A. Pinheiro *et al.*, "Parylene-Sealed Perovskite Nanocrystals Down-Shifting Layer for Luminescent Spectral Matching in Thin Film Photovoltaics," *Nanomaterials*, vol. 13, no. 1, 2023, doi: 10.3390/nano13010210.

[98] K.-L. Wong, J.-C. G. Bünzli, and P. A. Tanner, "Quantum yield and brightness," *J Lumin*, vol. 224, p. 117256, Aug. 2020, doi: 10.1016/j.jlumin.2020.117256.

[99] "Pecharsky, V. K., & Zavalij, P. Y. (2003). Fundamentals of powder diffraction and structural characterization of materials. Boston: Kluwer Academic Publishers.".

A Appendix A

A.1. Vacuum effect on perovskites film

While I worked on the project I tested a different type of exchange, using meshes that were predeposited with parylene to use as potential parylene source. I found a particular degradation of the perovskites film provoked by medium vacuum condition, in the order of some mtorr. Even for small times, around 1 hour, it was observed. It caused a decrease in PLQY and in absorbance. I put the samples under vacuum in a vacuum chamber and I measured the PLQY before and after the vacuum.

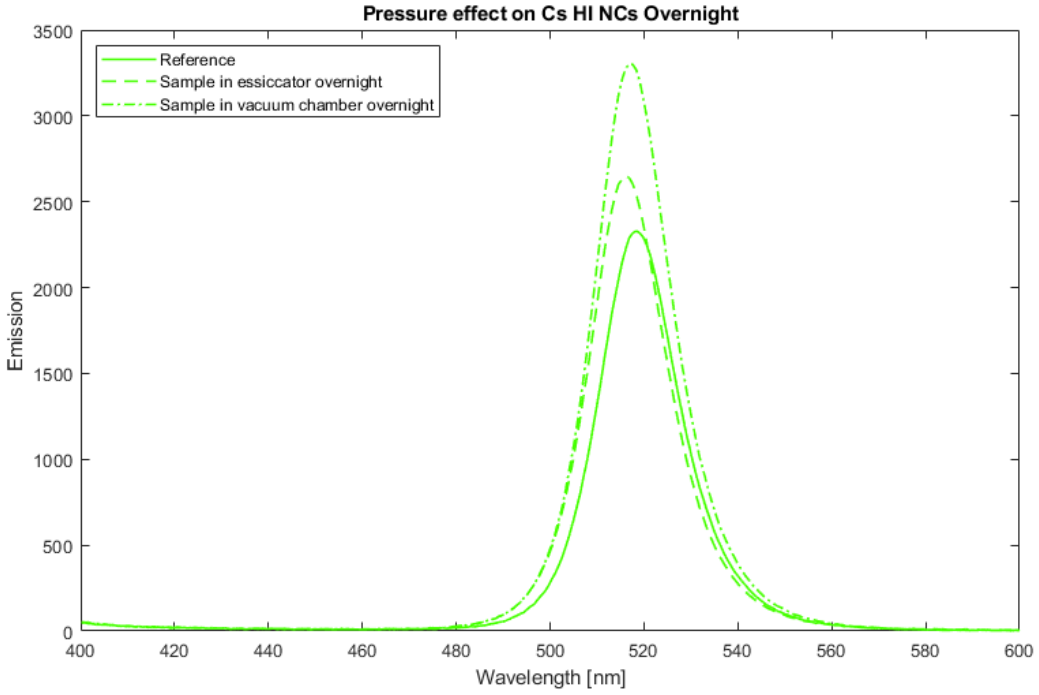

Figure A.1: $CsPbBr_3$ effect of Vacuum pressure. Essiccator pressure is higher than the vacuum chamber but still in the order of few mbarr.

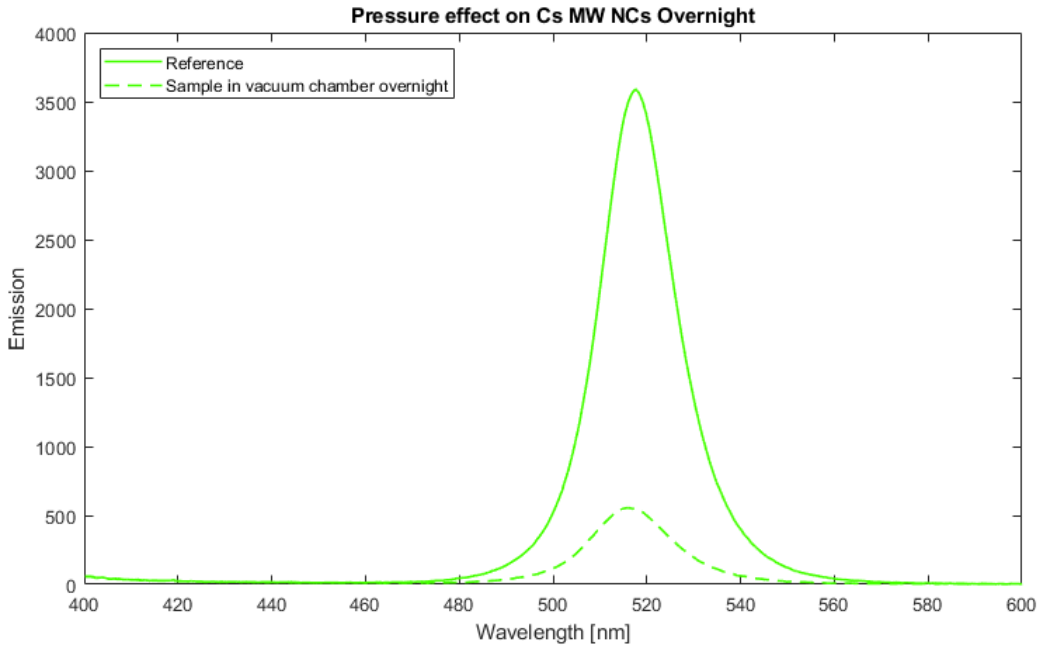

Figure A.2: $CsPbBr_3$ MW effect of Vacuum pressure.

Cs MW	PLQY measurement		
	PLQY	Absorbance	Wavelength
Reference	0.686	0.381	517.62
Sample in vacuum overnight	0.112	0.367	516.12

Table 9: PLQY values for Cs MW under vacuum

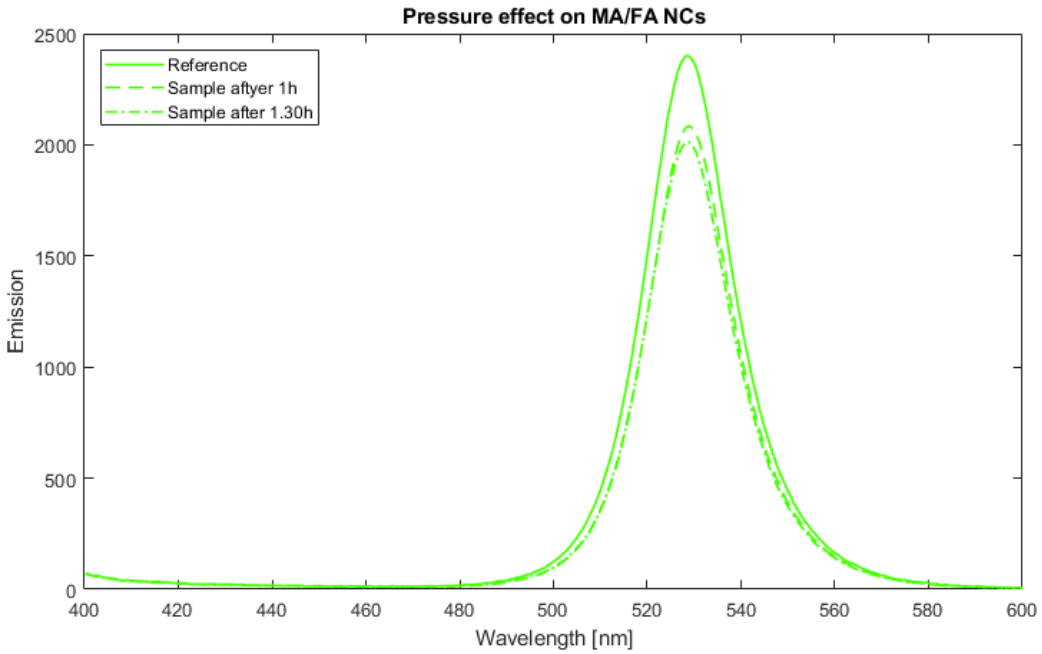

Figure A.3: MA/FA NCs under vacuum pressure of 3.5 mtorr for 1 and 1.30 h.

MA/FA	PLQY measurement		
	PLQY	Absorbance	Wavelength
Reference	0.833	0.266	528.86
1 h sample in vacuum	0.700	0.226	528.86
1.30 h sample in vacuum	0.669	0.222	528.86

Table 10: PLQY values for MA/FA under vacuum

B Appendix B

In this appendix can be found all the mathematical derivation and kinetic fitting used in the model.

B.1. Equations

The model is built as a plug flow reactor (PFR) that consider, a simultaneous deposition reaction along the channel and where only at the end the exchange reaction occurs. The exchange reaction is inserted in the model as a BCs at the end of the channel.

$$IN - OUT - CONS = ACC \quad \textbf{B.1}$$

$$IN = A_{cross} j_z \quad \textbf{B.2}$$

$$OUT = A_{cross} j_{z+dz} \quad \textbf{B.3}$$

$$CONS = A_{wall} K_{avg} (C - C_{wall}) \quad \textbf{B.4}$$

$$ACC = \frac{\partial (VC)}{\partial t} \quad \textbf{B.5}$$

Since that V is constant with respect to time, it can be placed outside. K_{avg} is the average mass transport coefficient in a tube with length dz.

$$A_{cross} = \frac{\pi d^2}{4} \quad \textbf{B.6}$$

$$A_{wall} = \pi d dz \quad \textbf{B.7}$$

$$V = A_{cross}dz \quad \textbf{B.8}$$

$$V = A_{cross}dz \quad \textbf{B.9}$$

$$j_z = -D\frac{\partial C}{\partial z} \quad \textbf{B.10}$$

After substituting all the equations inside B.1 and expanded j_{z+dz} the equation below is easy obtained:

$$\frac{\partial C}{\partial t} = D\frac{\partial^2 C}{\partial z^2} - \frac{4K_{avg}}{d}(C - C_{wall}) \quad \textbf{B.11}$$

Combining the multiplication factor with K_{avg}, K' is obtained. It has [1/min] as unit of measurement, so it is similar to a reaction rate. Considering that the polymerization is a free radical one, it can be considered that the monomer concentration at the wall is equal to zero. The final equation to solve is reported below:

$$\frac{\partial C}{\partial t} = D\frac{\partial^2 C}{\partial z^2} - K'C \quad \textbf{B.12}$$

The solver uses FDM discretization only for the partial derivative to z and uses an ode15s to solve it for all the time.

The BCs are:

$$C(z, t = 0) = C_0(z) \quad \textbf{B.13}$$

And for z:

$$C(z = 0, t) = C_F(t) \quad \textbf{B.14}$$

$$D\frac{\partial^2 C}{\partial z^2} = K_{exchange}C^n \qquad with\ z = L \quad \textbf{B.15}$$

Here, C_F (the feed concentration) is calculated from the process pressure using the ideal gas law and held constant at 1.12 mmol/L. C_0 (the initial channel concentration) is zero. The parameters $K_{exchange}$ and n are obtained by performing a linear regression of ln(Cl) against ln®, where Cl is the chlorine concentration in the sample and r is the reaction rate. The reaction rate is evaluated according to reaction time.

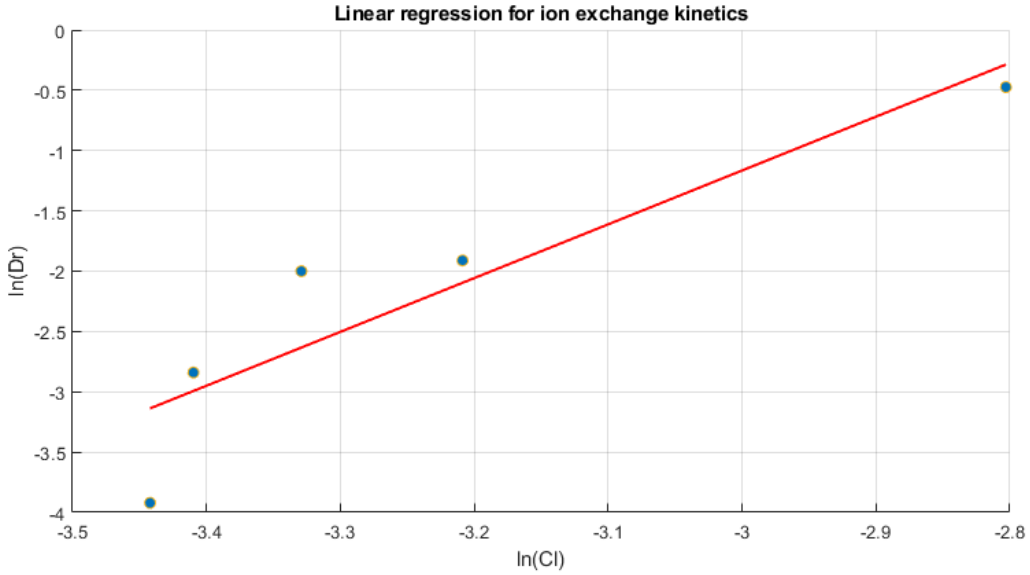

Figure B.1: Linear regression to find exponent and the kinetic constant.

N has be found to be 4.4608 and $K_{exchange}$ to be 2.0223e+05 1/min.

After these evaluation the last point was to find K'. Using experimental data has been possible to fit it in order to find a trend in function of channel length. The explanation is mentioned in Paragraph 3.3.

C Appendix C

This appendix explain how the denoising of Silicon peaks was performed.

Since the peaks of silicon wafer has always the same position thanks to the perfect crystalline structure of the wafer, the peak position can be used to reduce the noise. The XRD measurement has been performed using silicon substrate coated with perovskites by spin coating. Drop casting procedure was not possible due to inhomogeneity of the resulting film.

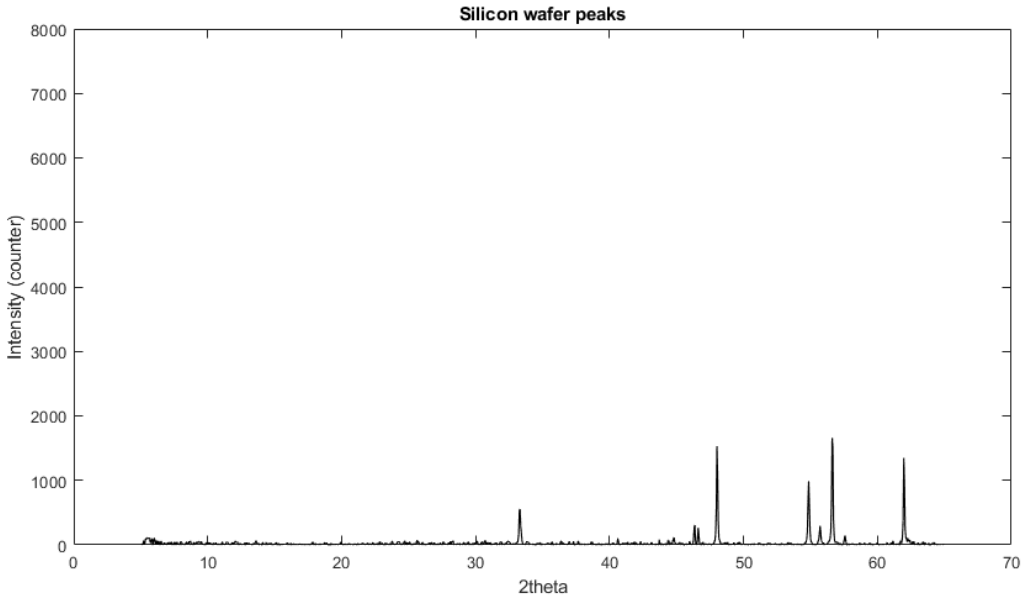

Figure C.1: XRD of Silicon wafer

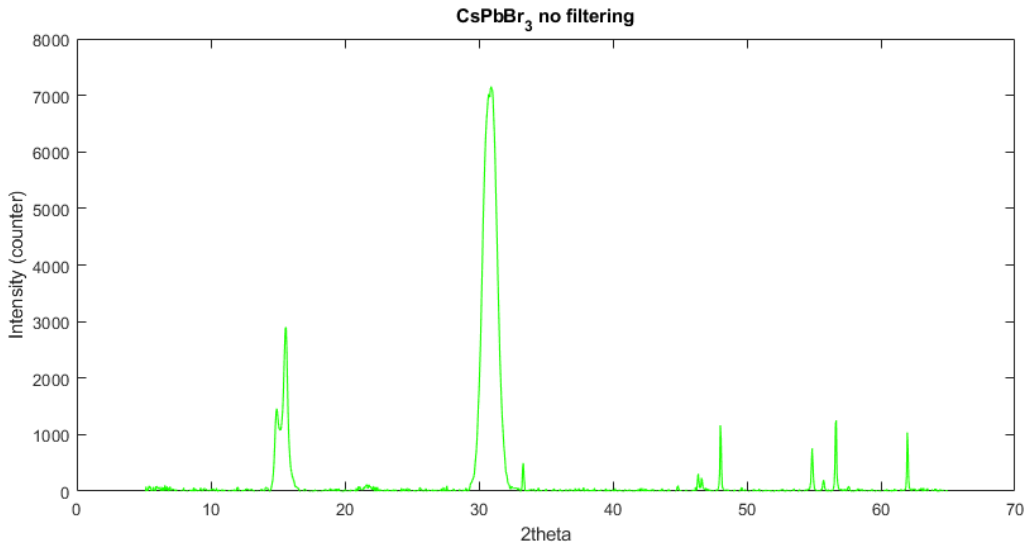

Figure C.2: XRD of $CsPbBr_3$ HI without Silicon filtering

As can be seen from Figure C.1 silicon peaks are only present after 32 degrees where $CsPbBr_3$ peaks are not anymore present. In that way has been possible to select the position of silicon peaks and decrease their intensity in plot of Figure C.2.

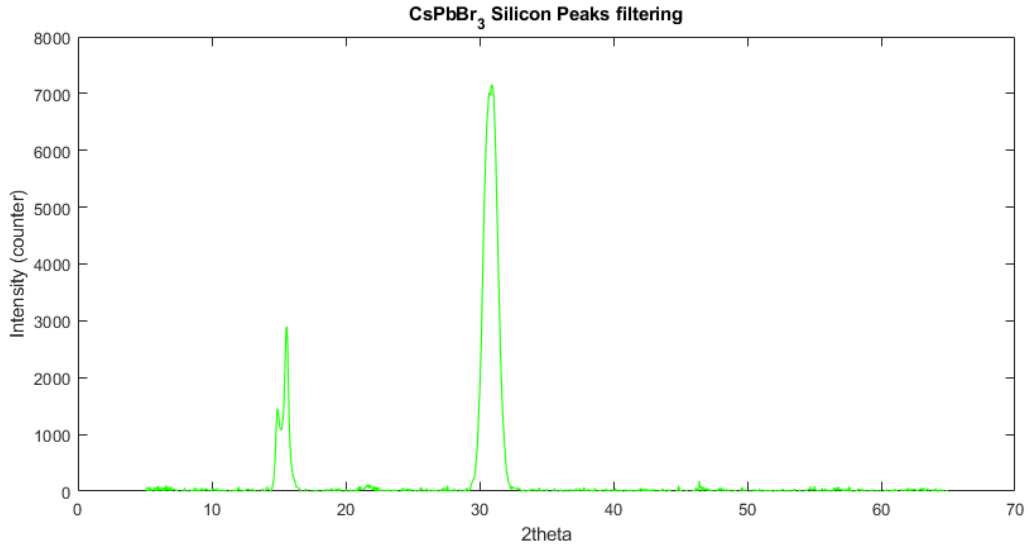

Figure C.3: XRD of $CsPbBr_3$ HI with Silicon filtering

The final result has been used also for the converted samples.

List of Figures

List if Tables

Acknowledgments

I would like to express my deepest gratitude to Professor Chih-Jen Shih for the opportunity to work in his research group at ETH. His support and guidance were more than invaluable.

Thank Ida a million for all the synthesis work she did for me and for her charisma that kept the lab brightened.

Thanks to Donato for providing the SEM images, for his understanding, and for all his help during the whole project.

I would like to thank also Gianluca for his profound insights in the data evaluation that helped a lot.

But most of all, I would like to thank Gerrit. His continuous support, endless patience, and enormous knowledge have been a cornerstone. He made me more flexible and nurtured my passion about this project.

Lastly, I want to thank the entire group for making this experience so exciting and memorable.